



UNIVERSITÀ  
DEGLI STUDI  
FIRENZE

## FLORE

# Repository istituzionale dell'Università degli Studi di Firenze

### **Preliminary design and fast prototyping of an Autonomous Underwater Vehicle propulsion system**

Questa è la Versione finale referata (Post print/Accepted manuscript) della seguente pubblicazione:

*Original Citation:*

Preliminary design and fast prototyping of an Autonomous Underwater Vehicle propulsion system / Allotta, Benedetto; Pugi, Luca; Bartolini, Fabio; Ridolfi, Alessandro; Costanzi, Riccardo; Monni, Niccolò; Gelli, Jonathan. - In: PROCEEDINGS OF THE INSTITUTION OF MECHANICAL ENGINEERS. PROCEEDINGS PART M, JOURNAL OF ENGINEERING FOR THE MARITIME ENVIRONMENT. - ISSN 1475-0902. -

*Availability:*

The webpage <https://hdl.handle.net/2158/1005055> of the repository was last updated on 2021-03-29T23:36:39Z

*Published version:*

DOI: 10.1177/1475090213514040

*Terms of use:*

Open Access

La pubblicazione è resa disponibile sotto le norme e i termini della licenza di deposito, secondo quanto stabilito dalla Policy per l'accesso aperto dell'Università degli Studi di Firenze (<https://www.sba.unifi.it/upload/policy-oa-2016-1.pdf>)

*Publisher copyright claim:*

Conformità alle politiche dell'editore / Compliance to publisher's policies

Questa versione della pubblicazione è conforme a quanto richiesto dalle politiche dell'editore in materia di copyright.

This version of the publication conforms to the publisher's copyright policies.

La data sopra indicata si riferisce all'ultimo aggiornamento della scheda del Repository FloRe - The above-mentioned date refers to the last update of the record in the Institutional Repository FloRe

(Article begins on next page)

# Preliminary design and fast prototyping of an Autonomous Underwater Vehicle propulsion system

Benedetto Allotta, Luca Pugi, Fabio Bartolini, Alessandro Ridolfi, Riccardo Costanzi, Niccolò Monni and Jonathan Gelli

## Abstract

The Mechatronics and Dynamic Modelling Laboratory of the Department of Industrial Engineering, University of Florence, as a partner of THESAURUS (Italian acronym for ‘TecnicHe per l’Esplorazione Sottomarina Archeologica mediante l’Utilizzo di Robot aUtonomi in Sciami’) project, has developed an innovative low-cost, multirole autonomous underwater vehicle, called Tifone. This article deals with the adopted methodologies for the autonomous underwater vehicle design: in particular, the main focus of this study is related to its propulsion system. According to the expected performances and requirements of THESAURUS project, the vehicle has to maintain good autonomy and efficiency (typical features of an autonomous underwater vehicle), with high manoeuvrability and hovering capabilities, which are more common of remotely operated vehicles. Moreover, cooperative underwater exploration and surveillance involve the use of a swarm of vehicles. In particular, the optimization of costs versus benefits is achieved through the design of a fleet of three multirole vehicles. Each autonomous underwater vehicle has five controlled degrees of freedom, thanks to four thrusters and two propellers: in this article, the preliminary design criteria concerning the vehicle and the design and testing of its actuation system are described.

## Keywords

Autonomous underwater vehicle, propulsion, magnetic transmission systems, fast prototyping, optimized motor design,

oil-pressure compensated actuators

Date received: 26 March 2013; accepted: 31 October 2013

## Introduction

The aim of this study is to describe the methodologies used for the design of an autonomous underwater vehicle (AUV) with particular attention to its propulsion system. Since the design of the propulsion system is deeply affected by the vehicle features and expected mission profiles, this article is organized in the following order:

Expected vehicle mission profiles. A brief description of the THESAURUS (Italian acronym for ‘TecnicHe per l’Esplorazione Sottomarina Archeologica mediante l’Utilizzo di Robot aUtonomi in Sciami’) project requirements, including some specifications of the expected vehicle mission profiles;

Vehicle hull design. Some general considerations concerning the design of the vehicle are introduced, to calculate the main hydrodynamic properties of

the hull, which are needed for a proper design of the propulsion system;

Design of the energy accumulators. Both the hull and the propulsion system design are mutually affected by the sizing of accumulators. A brief description of the available energy storage systems is introduced;

Design of the propulsion system. This part is focused on the propulsion system development describing the adopted design criteria, the simulation results and the experimental data from the preliminary testing activities.

---

Mechatronics and Dynamic Modelling Laboratory (MDM Lab),  
Department of Industrial Engineering, University of Florence, via di Santa  
Marta 3, 50139, Florence, Italy

Corresponding author:

Luca Pugi, MDM Lab, Department of Industrial Engineering, University of  
Florence, Via Santa Marta 3, 50139, Florence, Italy.

Email: [luca.pugi@unifi.it](mailto:luca.pugi@unifi.it)

## THESAURUS project

The aim of the THESAURUS project is to develop a class of AUVs able to cooperate in swarms in order to

perform navigation, exploration and surveillance of underwater archaeological sites. The project specifications are quite ambitious since the low-cost vehicles have to operate with a maximum depth of more than 300 m, an autonomy ranging from 8 to 12 h is required and a maximum speed of 5–6 knot has to be achieved. The total carried payload (excluding motors, batteries, navigation sensors and electronics) is quantified in about 30–40 kg and the cost of the vehicle has to be limited (less than 30,000–40,000 Euro), considering the lower budget available compared to military application. Low production and maintenance costs are a

mandatory specification of the project, considering the

necessity of producing several vehicles for a swarm composed of middle-sized vehicles whose commercial price is usually far higher. In particular, this last consideration forced the authors to choose self-design and assembly of vehicles from commercial low-cost components, which could be produced or acquired at even lower costs in the case of mass production. A first fleet of three different underwater vehicles, cooperating in a single swarm, is developed, as shown in Figure 1:

**Vision explorer.** A vehicle equipped with cameras, laser and structured lights for an accurate visual inspection and surveillance of archaeological sites. Visual inspection involves a short-range distance (few metres) between the vehicle and the target site and the capability of performing precise manoeuvring and hovering. Considering the mission profile specifications, a solution with through-body tunnel thruster, such as the C-SCOUT AUV, could be a good one;<sup>1,2</sup>

**Acoustic explorer.** Preliminary exploration of extended area to recognize potentially interesting sites involves the

use of acoustic instruments, such as side-scan sonar. Extended autonomy, and a stable and preferably noiseless behaviour have to be preferred. This kind of vehicle can perform longrange, extended missions. Consequently, navigation sensors able to compensate the drift of the inertial sensors, such as a Doppler velocity log (DVL), have to be installed on board. For this kind of activities, a vehicle with high autonomy and a smooth, noiseless behaviour can be the best solution, for example, REMUS 600;<sup>3</sup>

**Swarm coordinator.** A vehicle with extended localization and navigation capabilities is used to coordinate the swarm. This vehicle periodically returns to surface providing the global positioning system (GPS) and, more generally, detailed navigation information that can be shared with other vehicles of the swarm. This functionality should also be implemented by considering a cheaper, more stable surface vehicle as suggested by the authors in a previous study,<sup>4</sup> where different algorithms for the mutual localization of swarm vehicles have been proposed. Currently, the authors have adopted the following approach: when the mission area is quite defined and a surface vehicle or a buoy is available, coordination and data transmission are performed by this dedicated device. On the other hand, when a different operating scenario is required, one or more vehicles of the swarm could periodically interrupt their mission, performing the activity of a swarm coordinator.

Different mission profiles should correspond to different vehicle layouts suitable and optimized for a specific task; however, the authors, in accordance with the project requirements, have preferred a hybrid design able to satisfy different mission profiles, to reduce the engineering and production costs and to assure vehicle interchangeability. Each vehicle of the swarm can be customized for different mission profiles; this way the swarm composition could be altered, for example, two vehicles may be equipped for the visual inspection of a

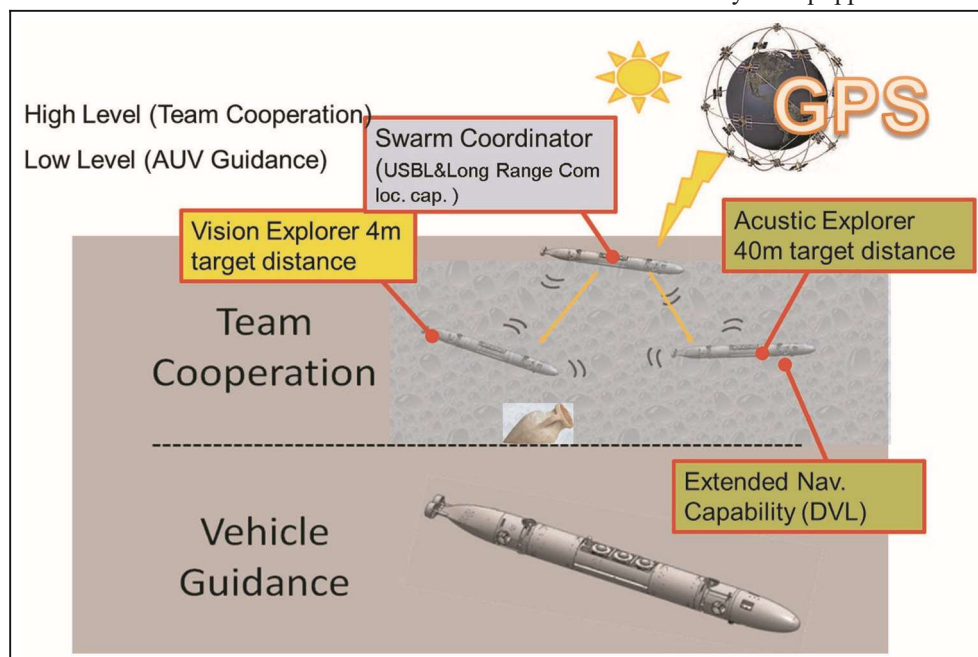


Figure 1. Examples of different mission profiles for the AUVs of the swarm.

AUV: autonomous underwater vehicle; GPS: global positioning system; DVL: Doppler velocity log; USBL: ultra short base line.

site. Since each vehicle differs only in terms of sensor layout and payload, the naval and electromechanical designs were focused on a common vehicle class, named Tifone. For instance, for an individual mission in which both acoustic and visual inspections of an archaeological site are performed by a single vehicle, the instrumentation layout described in Figure 2 can be easily assembled. The propulsion system is modular and merges different solutions adopted by existing AUVs<sup>3,5–10</sup> and hybrid gliders.<sup>11</sup> Since a prolonged mission autonomy is required, Tifone is designed with a torpedo shape, adopted by many existing AUVs. In Figure 3 and Table 1, a simplified scheme of the torpedo shape is shown, with the definition of the body-constrained reference system (Euler angle representation), which is typically adopted<sup>12</sup> to describe the vehicle kinematics and dynamics.

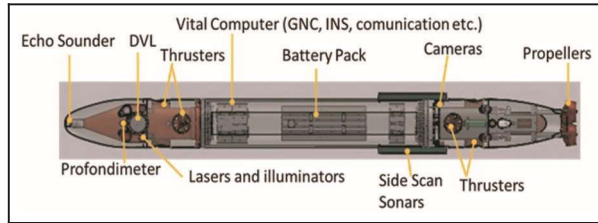


Table 1. Reference system (body constrained) and corresponding kinematical/dynamical variables.

Degree of freedom	Motion	Forces and torques, $\sim t$	Speed, $\sim n$	Position and orientation coordinates $\sim h$
1	Surge	X	u	x
2	Sway	Y	v	y
3	Heave	Z	w	z
4	Roll	K	p	f
5	Pitch	M	q	u
6	Yaw	N	r	c

Figure 2. Example of Tifone vehicle, customized for both acoustic and visual inspections of a site.

DVL: Doppler velocity log; GNC: guidance, navigation and control INS: inertial navigation system.

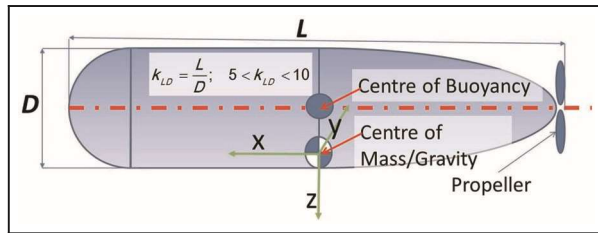


Figure 3. General shape and terminology of AUV Tifone.

between 6 and 8 as a compromise between the pressure skin friction losses and the pressure ones.<sup>14,15</sup> Many AUVs tend to be longer since additional payload is added by stacking up modular cylindrical modules.<sup>9</sup> However, since payload, hydrostatic lift and stored energy are roughly proportional to vehicle volume, an excessive slenderness could penalize these design aspects;

## Preliminary design of the hull

Considering the encumbrances of the payloads and the specifications of the project, the main dimensions of the vehicle are a total length of about 3 m and an external diameter of 300–320 mm, to be compliant with a limitation of the ratio  $L=D$  ('vehicle length over diameter') of about 10, quite common for torpedo-shaped vehicles. The limitation of  $L=D$  ratio arises from some hydrodynamic, structural and practical considerations:

**Hydrodynamic resistances.** From results available in the literature and practical considerations,<sup>13</sup> an increase of the  $L=D$  ratio over 10 considering a cylindrical or an axial symmetrical hull shape does not produce an appreciable improvement in terms of drags/resistances to motion. In particular, the optimal  $L=D$  ratio is often considered for values

**Structural design and transportability.** As the vehicle slenderness increases, the structural resistance of the vehicle with respect to the bending stresses introduced during the normal handling and transportation decreases, so it is not convenient to increase vehicle slenderness over a certain limit. More generally, the

transportability of a more compact vehicle is easier.

The shape of the vehicle was approximately optimized using the method proposed by Alvarez et al.<sup>5</sup> and then further optimized using a finite element model (FEM) developed with ANSYS CFX to increase as much as possible the efficiency and the autonomy of the vehicle, considering an external diameter of about 330 mm and a vehicle length of 3.3 m. In order to simplify the design and construction of the vehicle, a central cylindrical section of the vehicle of about 2 m was considered. As regards the shape of frontal tail sections, these were optimized considering a non-uniform rational B-spline (NURBS) surface. As clearly noticeable in Figure 4, the shape of the vehicle tail is not axial symmetric to better fit the layout of two propellers chosen for the vehicle.

Results from FEM calculations indicate a mean longitudinal drag coefficient  $C_{DX}$  of about 0.12, as shown in the results of Figure 4 and Table 2. Calculated values are quite near the ones proposed in the literature<sup>5,7,8</sup> for a vehicle with similar shape. However, it is also known from both the literature and the experi-

ence<sup>13,16,17</sup> that real drag forces are usually much higher compared to the prediction of the hydraulic resistance performed on a computational fluid dynamics (CFD) model of the hull shape. Also considering the variability of the shape and the encumbrances of carried payload, the authors used a precautionary value of the drag coefficient  $C_{DX}$  equal to about 0.35–0.4 for the design. The longitudinal resistance to motion  $X$  and drag coefficient  $C_{DX}$  are defined according to equation (1)

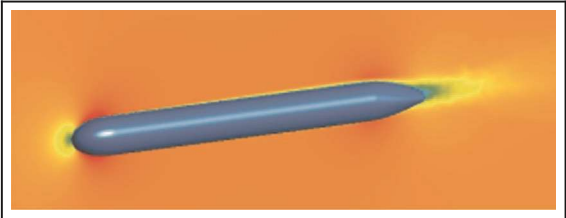


Figure 4. FEM model used for preliminary calculations of the drag coefficients: velocity field results.

Table 2. Calculated drag coefficients for different values of speed and Reynolds number.

Speed (m/s)	$F_{tot}$ (N)	$C_{DX}$	Re
1	12.54	0.1431	$3.310^6$
2	22.40	0.1278	$6.310^6$
3	31.16	0.1202	$9.310^6$
5	48.87	0.1115	$2.5310^7$

preferred a vehicle with a neutral behaviour, which complies with two conditions, as follows:

$$\frac{1}{X} = \frac{C_{DX} \rho u^2}{2} \quad (1)$$

Many AUVs described in literature are equipped with depth control tanks that can change the buoyancy of the vehicle and with mechatronic devices that can change the relative position of the centres of gravity and buoyancy, in order to modify the vehicle orientation.<sup>11,18</sup> However, in this project, the authors have

Vertical alignment of the buoyancy and the gravity centres has to be assured; a negative value of  $z_b$  is typically used to stabilize the vehicle against roll motions (3)

$$\frac{1}{V} \frac{dV}{dt} = \frac{r_v}{r_w} \quad (2) \quad x_b = y_b = 0; \quad z_b = -40 \text{ cm} \quad (3)$$

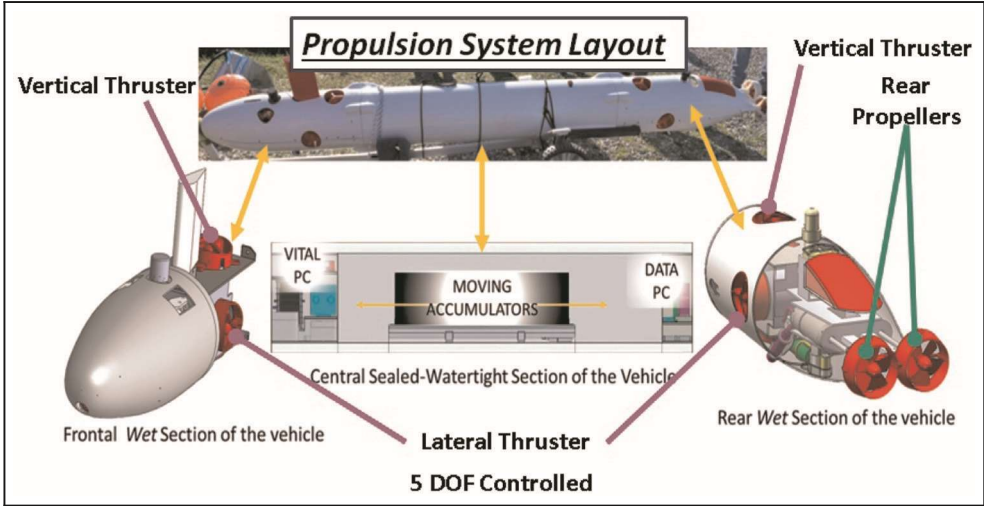


Figure 5. Vehicle and propulsion system design.  
DOF: degree of freedom.  
The mean vehicle density  $r_v$  has to be approximately equal to the saltwater one  $r_w$  (2);



where  $r$  is the local density and  $x_b$ ,  $y_b$  and  $z_b$  are the coordinates of the centre of buoyancy compared to a body-constrained reference system placed on the centre of mass of the vehicle. In order to adapt the vehicle to different sensor configurations and payloads, the hull has been designed according to the scheme of Figure 5.

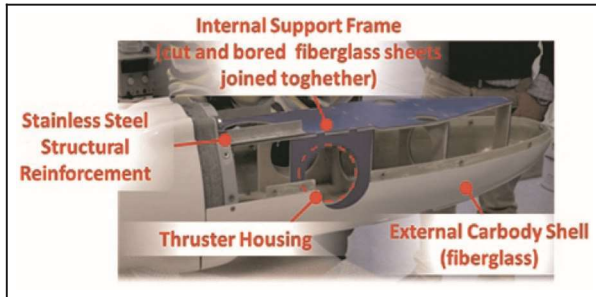


Figure 6. Fibreglass structure used for the design of the frontal and rear wet sections.

payload is divided into modular cases that can be Referring to the design described in Figure 5, the placed in different dedicated areas inside a central cylindrical watertight section. The central section has been verified using FEM for a maximum pressure of 70 bar (about 700 m of depth including buckling verifications) and successfully tested in water at a maximum depth of 300 m, as prescribed by project specifications:

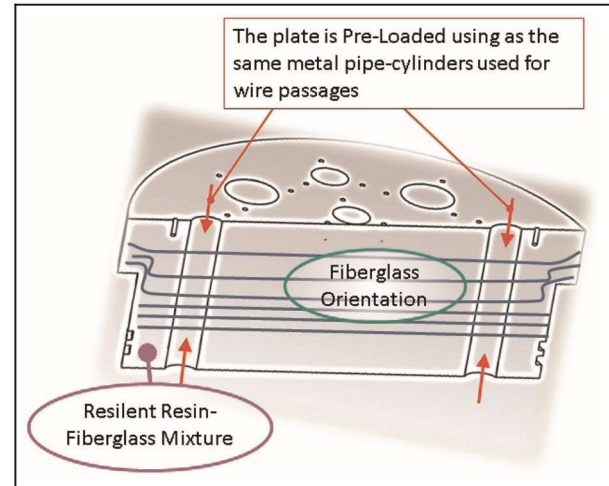
**Vital PC.** The vital computer and sensors manage the vital functions of the vehicle, for example, navigation and communication. This part of the vehicle is not a payload since it is mandatory to control the vehicle;

**Data PC.** It is the rack, which includes the electronic boards necessary for the data storage, sensor acquisition and signal conditioning. This electronic equipment is customizable but currently it is the same for all the vehicles;

**Customizable payload.** It defines different sensors and vehicle configurations. Cumbersome electronic boards could be placed in an additional case placed near the data PC. Wet sensors are placed in the frontal and rear sections of the vehicle, built using a light but rigid structure by adjoining fibreglass plates, as shown in Figure 6.

In addition, the caps at both ends of the central watertight cylinders are built using a composite fibreglass structure, which has been preloaded in order to increase structural stiffness and reduce the risk of crack growth, as shown in Figure 7. The resulting structure of the vehicle is quite light (about 40–50 kg) if compared with overall vehicle dimension, rigid and almost maintenance free, considering the extended use

of marine fibreglass and the use of stainless AISI 316L steel for minute parts. Also, the division of the vehicle into three detachable parts, which can be easily dissembled and transported separately, makes the handling and the transportation of the vehicle easier with respect to its size. Since the buoyancy of the vehicle has



to be optimized, the remaining volume of the hull will be filled with syntactic foam panels whose volume and dimensions could comply with the design constraints, given by equations (2) and (3). For a more precise Figure 7. Resilient/preloaded fibreglass caps.

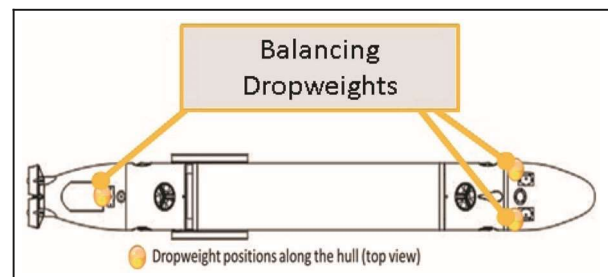


Figure 8. Position of the three drop-weights along the vehicle.

customization of the static balance of the vehicle, three drop-weights placed according to the scheme of Figure 8 should be easily adjusted. This way, in normal operating conditions (vehicle ballasted by dropweights), the vehicle is neutral with a slight additional buoyancy of about 1%22%, with respect to the one calculated from vehicle volume, to compensate compressibility of the hull at maximum depth<sup>19</sup> and to make the return to surface easier when state of charge of batteries could be lower; in the case of severe failure, the drop-weights (which are usually hold through a solenoid system) are released assuring an additional buoyancy of about 3%24% with respect to vehicle volume. In this way, in case of failure, a rapid return to surface is assured. Also the position of drop-weights enforces vehicle stability against rolling motions. Dropweights are assembled using iron-less bolts so their mass can be easily adjusted in order to compensate the variation of water density corresponding

to different operating scenarios, such as lakes, rivers or sea with different salinity. Finally, the neutral buoyancy behaviour and the inertial properties, which correspond to relations (2) and (3), can also be calibrated adjusting the axial position of the batteries along the hull since their mass is relevant and estimated as 20%–230% of the total vehicle weight, which is constrained by available buoyancy; most of the buoyancy is assured by the central watertight section so the maximum weight in air of the vehicle is constrained to not exceed 140 kg to stay neutral; considering the weight of structural components and host payload specifications, the weight remaining for batteries, propulsion system and onboard equipments is less than half of the total vehicle mass. Finally, for a vehicle of the class of Tifone, a stored energy between 3 and 6 kW h is highly feasible; as a consequence, since the energy density of commercial low-cost lithium-based accumulators is typically between 100 and 200 kW h/kg, the mass percentage of the batteries with respect to the total vehicle could be easily foreseen and constrained by current technological limits. These practical design considerations are confirmed also by studies available in the literature concerning the optimization of battery/vehicle mass ratio and its statistical value over a wide population of existing AUVs.<sup>20</sup> The position of the batteries is adjusted using a screw transmission system actuated by an electric motor, as shown in Figure 5. This way, it is also possible to statically control vehicle pitch orientation without activating any additional actuator. Also a slight modification of the pitch angle in comparison with the travelling direction can be used to correct the vehicle depth with a moderate energy consumption with respect to the use of additional thrusters or actuators. This solution has been adapted from glider<sup>21</sup> and hybrid glider technology.<sup>11,18</sup>

## Accumulators and energy management system

From preliminary studies on the vehicle hull, it has been possible to approximately evaluate the drag coefficients of the vehicle and roughly estimate the needed amount of energy, since the required power depends on the efficiency of the propellers, motors and transmission system. The power needed by the propulsion on-board systems and payloads was approximately known (about 350 W), so considering a mission duration of about 8–10 h, it was possible to calculate the needed energy in about 3–3.5 kW h.

In particular, the value of 350 W was calculated considering the sum of the following contributions:

- Propulsion power. About 100–200 W, depending on the mission profile and speed;
- Vital navigation functions. About 50–60 W is the estimation of power consumption due to on-board vital instruments that have to be fed to assure the minimal

navigation and localization functions (vital PC, depth and inertial sensors, magnetometer and so on);

Hotel load. A continuous/mean contribution of about 100 W is considered. This value is quite sensitive to the mission profile, especially considering the multirole capabilities of the vehicle: for example, for visual inspection of the site, higher peak

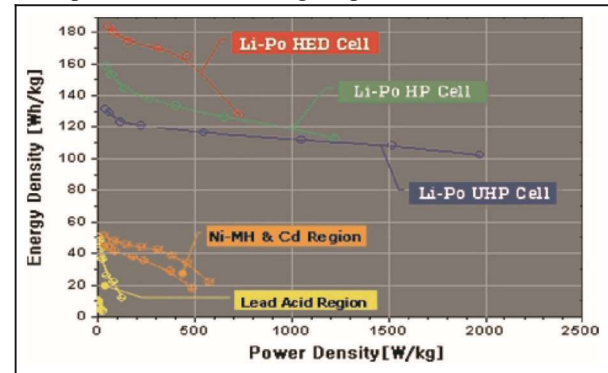


Figure 9. Li-Po batteries performance compared to different accumulator technologies.

consumptions of power due to the illumination of the target should be considered, while for prolonged acoustic inspections, the power demand should be more continuous.

As the installed power was quite high, it was decided to elevate the nominal voltage of the accumulators to 48 V, which represents a good trade-off among the different technical issues, such as the reduction of the electrical losses and the troubles related to insulation and protection of low-voltage equipments (generally easier to be assembled and found with low-cost commercial components). In order to maximize the capacity of the energy storage system, lithium-polymer (Li-Po) batteries, which have higher energy capacities<sup>22</sup> compared to other kinds of cheaper commercially available accumulators, as shown in Figure 9, have been chosen. Furthermore, Li-Po technology drastically reduces the risk of explosions usually associated with the traditional Li-ion batteries. As shown in Figure 9, the design of Li-Po batteries may be optimized to satisfy different power–energy specifications:

High-energy density (HED). Accumulators designed to maximize energy density corresponding to minimal encumbrances and weights;

High power (HP) and ultra-high power (UHP).

Accumulators suitable for higher currents.

Tifone AUV does not require high currents, so theoretically, HED accumulators may be the best choice; however, for reliable and practical use, HP Li-Po batteries support higher charging currents, which make the vehicle use and its maintenance easier and faster. Besides, from a commercial point of view, HP Li-Po

batteries are widely diffused and available since they are used for many applications, such as electric cars and sport vehicles; ultimately, they were preferred to the HED ones. The chosen layout involves the use of two packs of batteries whose features are shown in Table 3 for a total power of 3.84 kWh, which is enough in conformity with the specifications, even considering Table 3. Main features of a single battery pack.

Cell producer	Kokam assembled by Egraftech	Maximum discharge current	30 A
Nominal voltage	48.1 V (3.7 V 3 13)	Maximum charge current	10 A
Cut-off voltage	35.1 V (3.7 3 13)	Current capacity	40 Ah
Maximum voltage	54.6 V (4.2 3 13)	Total encumbrances	mm 230 3 260 3 150 (h)
Layout	13 Cells series connected	Total weight	About 14–15 kg
BSM: battery management system	On board		

## Propulsion system

In Figure 5, a simplified scheme of the proposed layout for the propulsion system is shown: linear motions along x–z directions, and pitch and yaw rotations are directly controlled by a system of actuators composed of two main propellers (longitudinal) and four thrusters

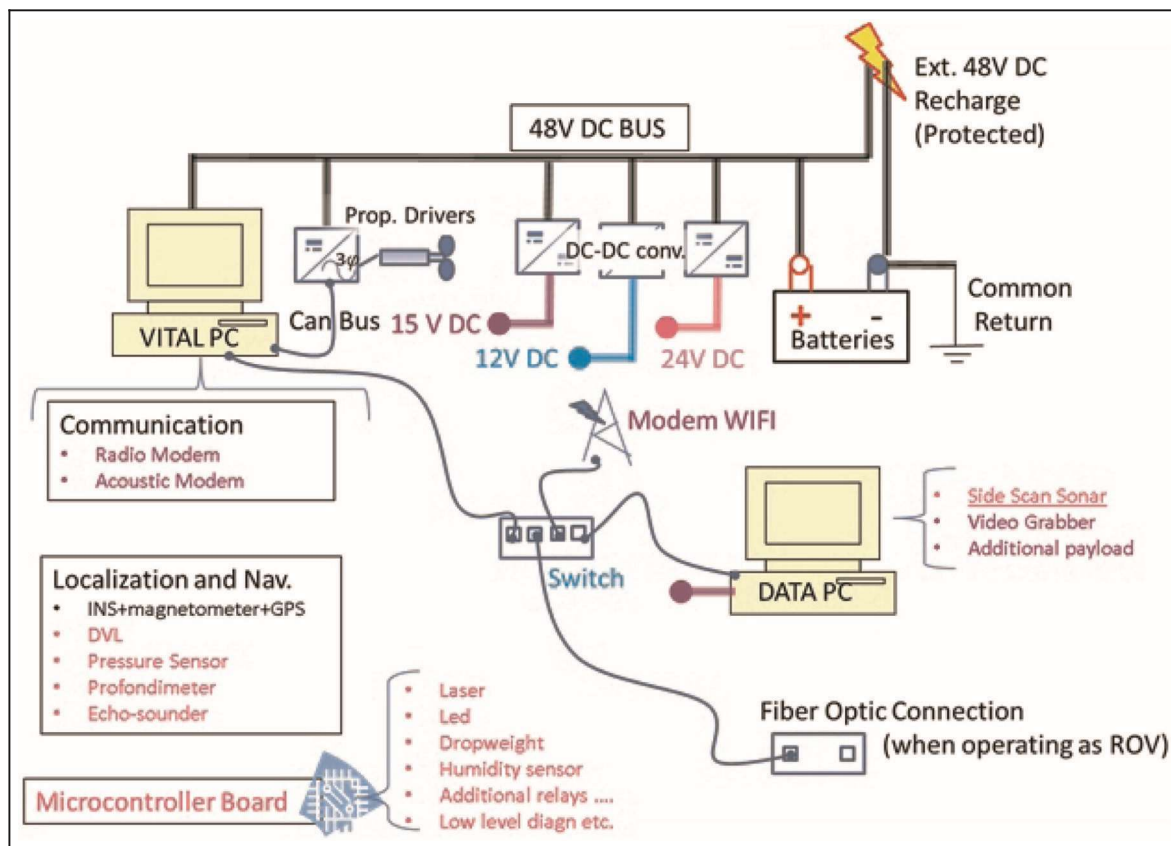


Figure 10. Simplified scheme of the internal electric plant of the vehicle.

DC: direct current; GPS: global positioning system; DVL: Doppler velocity log; ROV: remotely operated vehicle.

a performance degradation of 10% due to ageing or incomplete/fast recharge (Table 3). Since a low amount of power, corresponding to less than 10%230% of the total stored energy (linked to the different mission profiles), is required by low-voltage utilities, additional direct current (DC)–DC converters (stepdown choppers) are added to the power system, according to the needs of the different installed components, as shown in the scheme of Figure 10.

(vertical and lateral). As previously described, the position of the accumulators can be continuously modified to control the vehicle pitch. This particular layout of the propulsion system is adopted mainly to adapt the vehicle to the different mission profiles, without penalizing efficiency and usability:



Hovering precise low-speed manoeuvring. Lateral and vertical through-body thrusters assure good hovering capabilities and a very good handling, which can be quite useful, for instance, for a visual inspection of the site. Through-body thrusters are often used for this reason on many AUVs, for example, in C-Scout<sup>23</sup> or over-actuated configuration in synergy with control surfaces;<sup>24,25</sup>

Stable and energy-efficient motion for prolonged missions. The use of the through-body thrusters should be minimized when the vehicle has to travel at cruising speed for a prolonged time, for example, in the case of acoustic missions. In this case, the activation of the thrusters may be avoided mainly for two reasons:

Energy efficiency. The thruster efficiency is quite low and it is further degraded especially in the presence of crossflow as stated by many theoretical and experimental studies available in the literature;<sup>1,27,28</sup>

Turbulence and noise. The activation of the thrusters could produce turbulence and noise. The reaction torques of the motors might introduce disturbances, perturbing the vehicle's smooth motion.

For this reason, when the vehicle is travelling at cruising speed, the yaw motion is controlled differentiating the rotation speeds of the left and right rear propellers, while the pitch attitude, and consequently the depth, is controlled by adjusting the position of the batteries:

Minimization of control surfaces such as rudders and stabilizing fins. These parts are prone to accidental ruptures, jamming and other troubles and often have to be removed or protected when the vehicle has to be transported. With the chosen layout, the authors have tried to minimize their use;

Vehicle stabilization. The vehicle is under-actuated considering the roll motion. The roll angle is stabilized only by the static (hydrostatic) attitude of the vehicle. Using two counter-rotating rear propellers, the disturbances introduced by the reaction torques are minimized. This feature is very useful in all applications where the angular alignment between the vehicle and the inspected site has to be assured. The propellers of the lateral and vertical thrusters are also counter-rotating to reduce disturbances due to the reaction torques in the hovering phase;

Simplification of power electronics and control. The whole propulsion system, including the control of the battery position, is performed by seven configurable controlled drivers (Elmo whistle 15–60 or Elmo whistle 20–60) whose features (size, producer and communication protocol) are the same. This way, it is possible to drastically simplify the design, construction programming and maintenance of vehicle power electronics. For the six power drives controlling rear propellers and thrusters, the maximum peak power

requirement is quantified at about 200 W. The same drives and motors could be easily configured for a position control loop (motors with integrated encoders and drives with configurable position loop), so the same electronic and electric hardware may also be used to control the position of a rudder or any other kind of navigation/control

surfaces of the vehicle;

Simplified mechanical design. Also the diameter of the propellers and thrusters are the same (120 mm), and it is maximized with respect to available encumbrances to improve the efficiency. This way, many aspects concerning the design and preliminary testing of the system are quite simplified (e.g. compared to more complex solutions such as the podded thrusters or trolling motors).

### Preliminary design of rear propellers

Since both the diameter (120 mm) and the available power (200 W) for rear propellers were substantially assigned, the authors had to optimize their design considering the shape of the profiles and in particular the ratio between pitch  $p$  of the screw and diameter  $d$  of the propeller. The rear propellers are ducted with a 19 A accelerating nozzle.<sup>29</sup> The nozzle is adopted to protect each rear propeller from dangerous contacts with seaweeds, or other suspended solid bodies, and to increase the bollard thrust. A further non-secondary aspect was the safety, since the covering provided by the nozzle partially protects the undertrained user, such as university students, from potentially dangerous contacts with the rotating propeller. For the design of the propeller, the authors started from  $K_a$  4-70 and  $K_a$  5-75 propellers since experimental data concerning their behaviour as ducted propellers with 19 A nozzle were available from the literature.<sup>30,31</sup> In particular, there were also available information concerning their behaviour in terms of four quadrant operations for the  $K_a$  4-70. In Figure 11, as an example, the behaviour of several  $K_a$  4-70 propellers (first quadrant operation) with different  $p=d$  ratios are shown.

$K_i$ ,  $K_q$ ,  $A_r$  and  $h$  are defined as functions of the advance coefficient  $J$  according to the following equations

$$J = \frac{V_a}{nd} (\text{advancecoeff:}) \quad \delta 4p$$

$$\underline{T}$$

$$\begin{aligned}
K_q &= \frac{Q}{A} r n^2 d^5 \text{ (torquecoeff:)} & \delta 6p \\
A_r &= \frac{A}{A_d} \text{ (arearatiocoeff:)} A_d & \delta 7p \\
h &= \frac{K_t(J) J}{K_q(J)^2 p} \text{ (efficiency) } V & \delta 8p \\
K &= \text{(thrustcoeff:)} & \delta 5p
\end{aligned}$$

where  $n$  is propeller speed (Hz);  $r$  is density ( $\text{kg/m}^3$ );  $Q$  is torque (N m);  $T$  is thrust (N);  $A_p$  is propeller area ( $\text{m}^2$ ) and  $A_d$  is disc area ( $\text{m}^2$ ). According to equation (8), the efficiency of the propeller  $h$  is a function of the advance coefficient  $J$  of the propeller and consequently of the vehicle. In the hypothesis of a constant drag coefficient  $C_{DX}$  of the vehicle, the steady-state resistances to a longitudinal motion are roughly proportional to the squared speed  $u$  with respect to water as stated by equation (9)

$$X = \frac{1}{8} C_{DX} r p D u^2 = k_x u^2 \quad \delta 9p$$

$k_x$  is a coefficient of proportionality ( $k_x = \frac{1}{8} C_{DX} r p D^2$ ), which can be assumed roughly constant neglecting the variation of drag coefficient  $C_{DX}$ , vehicle diameter  $D$  and finally water density  $r$ . In the case of vehicle straight motion assuming inlet speed  $V_a$  equal to vehicle one  $u$  (propeller flux unperturbed by hull passage), equation (9) could be rewritten in the following form

$$X = k_x u^2 = k_x V_a^2 = k_x J^2 n^2 d^2 \quad \delta 10p$$

In steady-state conditions, the equilibrium between longitudinal drag forces ( $X(J)$ ) and thrust of each propeller ( $T_i(J)$ ) has to be verified (equation (11)), where  $n_{\text{prop}}$  is the number of identical propellers working in parallel (in the proposed application  $n_{\text{prop}}=2$ )

$$X(J) + \sum_{i=1}^{n_{\text{prop}}} T_i(J) = 0 \quad \delta 11p$$

From equation (11), exploiting the definitions of coefficients  $K_t(J)$  and  $J$ , equation (12) can be obtained

$$X(J) = k_x J^2 n^2 d^2 = \sum_{i=1}^{n_{\text{prop}}} T_i(J) = K_h n_{\text{prop}} K_t(J) r d^4 n^2 \quad \delta 12p$$

where  $K_h$  is an additional efficiency coefficient ( $K_h \leq 1$ ), considered to take into account the perturbation of the propeller velocity field due to the vehicle hull passage (including vortex shedding effects).

Feasible values of  $K_h$  for a first draft design should be taken from Carlton.<sup>29</sup>

Solving equation (12) with respect to  $J$ , it is possible to find a solution  $J$ , which corresponds to the steady-state value of the advance coefficient considering the interaction between the propellers and the vehicle.

Consequently, the steady-state values of thrust, torque and efficiency coefficient,  $K_t(J)$ ,  $K_q(J)$  and  $h(J)$ , can be calculated. The chosen propulsion layout is optimal as the calculated efficiency for the steady-state condition is approximately equal to the maximum possible  $h_{\text{opt}}$  for the chosen propeller family as stated by equation (13)

$$h(J) h_{\text{opt}} = h(J_{\text{opt}}) \quad \delta 13p$$

where  $J_{\text{opt}}$  represents the value of the advance coefficient corresponding to the maximum efficiency.

$K_t(J)$  behaviour is described by monotonically decreasing curves, as shown in the example of Figure 11, which should be often approximated by linear functions described by equation (14)

$$K_t(J) / K_{t,b} = \frac{J_{\text{null}} - J}{J_{\text{null}}} = K_{t,b} \frac{J_{\text{null}} - J}{J_{\text{null}}} \quad \delta 14p$$

where  $J_{null}$  represents the no-load advance coefficient at which the delivered thrust of the propeller is equal to 0 and  $K_{tb}=K_t(0)$  is the value of the thrust coefficient calculated for a null advance coefficient (Bollard thrust).

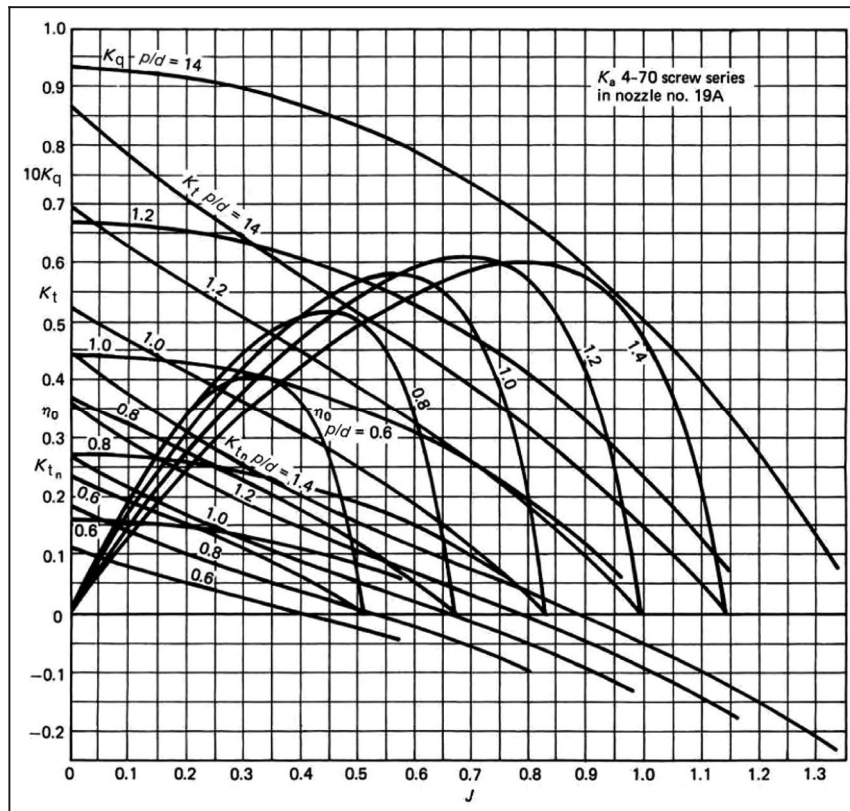


Figure 11. Examples of  $K_t(J)$ ,  $K_q(J)$  and  $h(J)$  curves considering the contribution of the nozzle.<sup>29</sup>

Value of  $J_{null}$  is approximately proportional to propeller  $p=d$  ratio through a near-to-unitary coefficient  $k_{null} p$

$$J_{null} \propto k_{null} p$$

Also  $K_{tb}$  value for propellers of the same series is an increasing monotonic function of propeller  $p=d$  ratio. Merging the steady-state equilibrium described by equation (12) with the linearized propeller model (equation (14)), equation (15) can be obtained; equation (15) can be easily solved as a function of  $J$  in order to find  $J$ , since it is a parabolic curve with constant coefficients

$$k_x J + \frac{2}{\delta_{15} p} \frac{K_h K_{tb} r d^2}{J^2} - k_{null} p = 0$$

A parametric study of  $J$ , calculated as the positive solution of equation (15), is useful to have qualitative common-sense considerations, well known among naval/marine engineers

Higher values of drag resistances  $k_x$  involve lower values of  $J$ ;

For propellers of the same series, an increase of  $p=d$  usually involves an increase of the thrust coefficients  $K_t$  and consequently a higher value of calculated  $J$ .

Since the value of optimal advance coefficient  $J_{opt}$  is roughly proportional to propeller  $p=d$  ratio, the following practical considerations are taken into account:

Large or low-efficiency hull design associated with higher  $k_x$  and lower  $K_h$  involves the use of propeller with lower  $p=d$  ratio;

As the equivalent propeller disc area  $A_{eq} = (n_{prop} p d^2) / 4$  increases, higher  $p=d$  ratio should be adopted.

Since the motion resistances of the vehicle are approximately known, using  $K_t$ ,  $K_q$  and  $h$  curves for Kaplan propeller,<sup>29</sup> the authors could choose an optimal  $p=d$  ratio for the rear propellers of about 1.2–1.4 considering a five-blade propeller configuration, derived from the original geometry of a  $K_a$  5-75 propeller. Installing a variable pitch propeller, it could be easier to customize and optimize the blade profiles with respect to the vehicle drag resistances and desired performances. However, the authors preferred a simpler and cheaper solution with fixed pitch propellers. The propellers were driven by permanent magnet brushless motors, which were originally Faulhaber (mod. 44–48) with an epicycloidal gearbox (1:5 reduction ratio) produced by Gisin. The efficiency of the gearbox was evaluated about 80%–90% (85% was the nominal value suggested by the manufacturer). As shown in Figure 12, the nominal power

of the motor is delivered in a very narrow range of velocities (8000–10,000 r/min of the

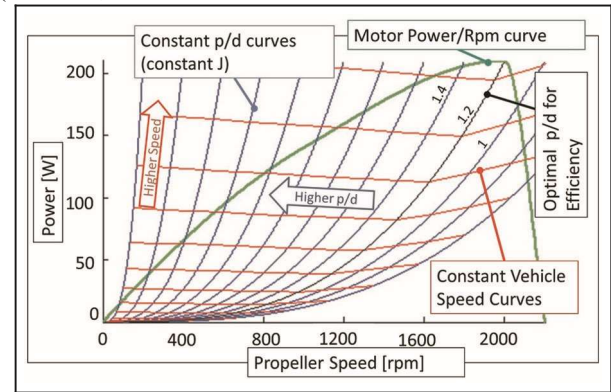


Figure 12. Optimization of propeller design considering both the vehicle advance resistances and motor performances. RPM: revolutions per minute.

motor corresponding to 1600–2000 r/min of the propeller shaft).

This problem that is common to most of the conventional brushless motors available in commerce is that the coupling between the motor and the propeller should be carefully evaluated and optimized. The authors solved this problem by adopting fast prototyping techniques, which allow to produce, in a few hours, several propellers with different geometries (different blade profiles,  $A_r$ , and so on) at affordable costs. The propeller design was slightly modified in order to easily create a prototype using the Stratasys three-dimensional (3D) printer of the MDM Lab. In particular, the thickness cord length ratio was increased to improve the fatigue and the bending resistance, considering the used polymeric material (Acrylonitrile Butadiene Styrene (ABS)) whose mechanical properties and duration are limited but compatible with the mission duration and the limited production costs. From preliminary calculations (results were shown in Figure 12), it was possible to verify that an optimal coupling of the propeller with respect to motor power corresponds with current data to a  $p=d$  ratio value between 1 and 1.4. The chosen profiles, quite similar to a  $K_a$  5-75, were designed to compensate the technological limits of the plastic material (ABS) used by the fast prototyping machine:

A number of blades was chosen to improve the mechanical endurance and reliability of the propeller especially considering the fatigue to which the material is subjected (anisotropic mechanical properties deriving from the particular building process consisting of the deposition of plastic on the planar sections);



More specifically, the profile thickness especially at the basis of the blade was enlarged (higher resistance to bending); all filleting radii were increased; for this operation, it was easier to produce the chosen profile by modifying an original geometry corresponding to a Ka 5-90 profile.

The response of the propeller should be optimized in order to be quite insensitive to the sign of the rotating speed. In a few words, the design has to be optimized for four quadrant operations;<sup>31</sup> the

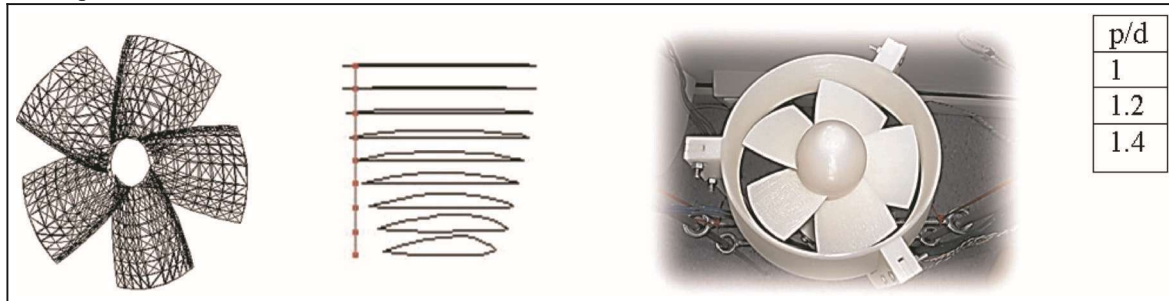


Figure 13. Fast prototyping of propellers from CAD model to ABS prototype.

Propellers with a different  $p=d$  ratio, covering a range from 1 to 1.4, were created, as prototypes, to optimize the coupling with the chosen electric actuator and to verify the preliminary design. In Figure 13, a propeller computer-aided design (CAD) and the corresponding plastic prototype are shown.

In particular, in Figure 13, the different phases of the manufacturing workflow are visible:

Blade profiles are created over concentric cylindrical surfaces using reference data for the desired profiles.

3D curves can be produced using dedicated software or simply generated using self-made MATLAB scripts. The generated curves are automatically loaded to a parametric CAD (such as SolidWorks, Solid Edge or ProEngineer) to automatically generate the 3D construction frames. In this phase, the blade profile can be radically customized:

NURBS surfaces interpolating the 3D blade profiles are designed in order to pass from a wireframe to a trimmed surface representation. Finally, the surfaces are converted into a boundary representation (B-Rep) solid geometry. The B-Rep geometry of the blade could be used in a conventional parametric CAD to generate solid representation of the desired component including, for example, mechanical interface with the propeller shaft;

The solid representation component is converted into a meshed stereolithography (STL) format, which could be used as an input for the integrated computer-aid machining (CAM) software of the 3D printer to optimize production parameters.

typical accelerating nozzle and all the design criteria of the blade profile suitable to optimize the efficiency in a preferential rotation sense should not be used. For the adopted symmetric blade profiles, there are few experimental data available and a general lack of systematic curves for an optimal sizing. Consequently, the thruster blade profiles have to be tested experimentally to verify their real performances. Also, in this case, the different profiles, which mainly differ concerning  $p=d$  ratio, have been produced in ABS using fast prototyping machines;

The lateral and vertical thrusters are used to control lateral, vertical and turning motions of the vehicle. The resistances associated with a pure lateral motion of the vehicle are far higher compared to the longitudinal ones. The resistances associated with vehicle rotations or mixed motion are lower. Variable motion resistances lead to a non-optimal design of the thruster from an efficiency point of view; however, even considering the above-cited uncertainties, it is quite clear the use of lower  $p=d$  ratio for thruster blades, compared to the longitudinal propeller one, is highly advisable;

The encumbrances and the weight reduction are more important than efficiency considering a typical mission profile in which the use of the thrusters may be intermittent, limiting the amount of the consumed energy;

## Lateral and vertical thruster design

Lateral and vertical bow thrusters have been introduced to control the corresponding motions and rotations of the vehicle. As they have a different use compared to the propellers, the design requirements are slightly different:

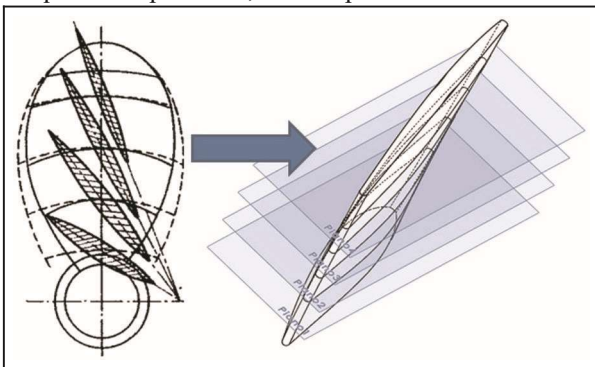
engineering topic, and some references can be found in the literature.<sup>28,31–34</sup> Typically, the proposed propeller profiles are symmetric and their shapes are designed using simple ellipse or parabolic profiles; such profile geometry is further simplified considering limitations and constraints deriving from the adopted fast prototyping technology (mechanical tolerances, general workability and mechanical properties of used materials). In Figure 14, a typical blade profile and the adopted one are shown.

### Transmission system, sealing and thermal issues

The motors have to operate at more than 300 m depth: an external pressure of the water of over 30 bar has to be compensated, so the sealing of the actuator is a demanding task. Different solutions are proposed for an optimal design of the actuation system, as shown in the simplified scheme of Figure 15:

Finally, since the efficiency is not the most important feature, a lower  $p=d$  ratio (0.6–1) has been deliberately chosen to increase the thrust and conversely acceleration and manoeuvring properties of the vehicle at lower speed, considering the typical behaviour described in Figure 12. It is also worth noting that through-body thrusters has to be used and consequently optimized for hovering and, more generally at very low speed, when the vehicle is submerged; in fact, their efficiency, as stated in many studies available in the literature,<sup>21,23,24</sup> dramatically decreases in the case of relevant crossflows and when the vehicle is near the surface (as a consequence of both cavitation and severe off-design conditions).

The design of the thrusters, able to operate considering four quadrant operations, is an important



Contactless magnetic transmission. The torque between the actuator and the propeller is transmitted using a contactless magnetic joint. There are different types of joints according to the chosen flux direction, which can be axial or radial as stated by theoretical and experimental works available in the literature.<sup>36,37</sup> Typical layouts of magnetic joints used for this kind of applications are shown in Figures 16 and 17. With this transmission system, the sealing of the motor is drastically simplified since no shaft has to pass through the walls of the sealed sections;

Oil-filled actuator. Actuators are filled with dielectric oil in order to balance the structural stresses induced by the external pressure. The use of oilcompensated components (motors, batteries and electronic boards) to resist to high pressure is commonly adopted by many vehicles, for example, Autosub 6000.<sup>10</sup> The hydrostatic pressure of the oil compensates the external pressure of the water; the

Figure 14. Symmetric blade profiles for 4Q operations: typical profiles<sup>32</sup> and simplified geometry adopted.

difference between the internal oil pressure and the external one is quite small since the motor is hydraulically connected to a flexible pipe capacity whose stiffness against the external pressure is negligible, as shown in Figure 15. The elastic pipe works also as a rough oil accumulator able to compensate losses or volumetric changes induced by the external pressure and temperature conditions.

### Design of the magnetic transmission system

In order to properly design the magnetic joint, the authors started from formulas known in the literature used to calculate the torque transmitted by joints whose polar expansions are shaped as cylindrical sectors.<sup>36,37</sup> First, the equations were implemented in MATLAB; using these equations, it is possible to roughly design a

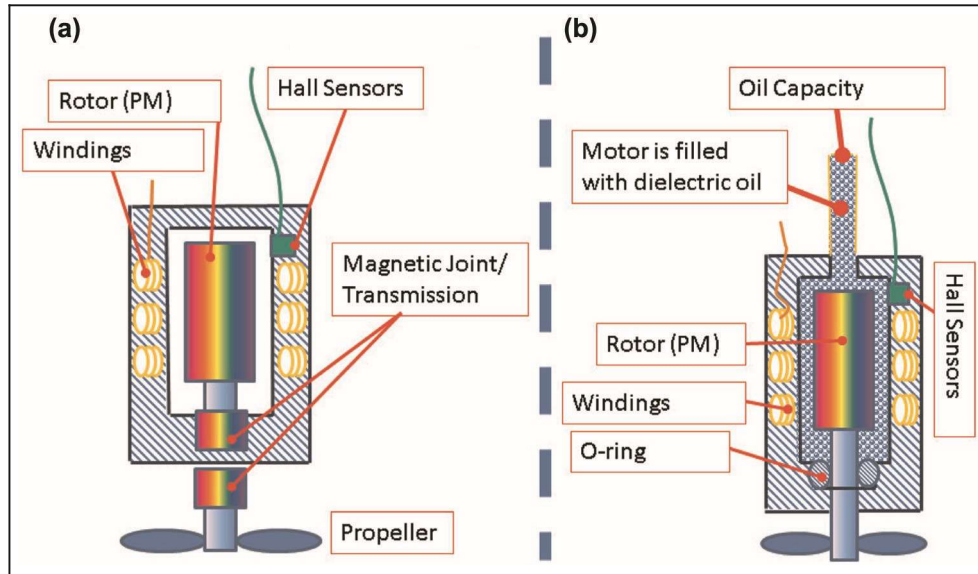


Figure 15. Comparison between an actuator with (a) sealed motor (magnetic transmission) and an (b) oil-filled actuator.

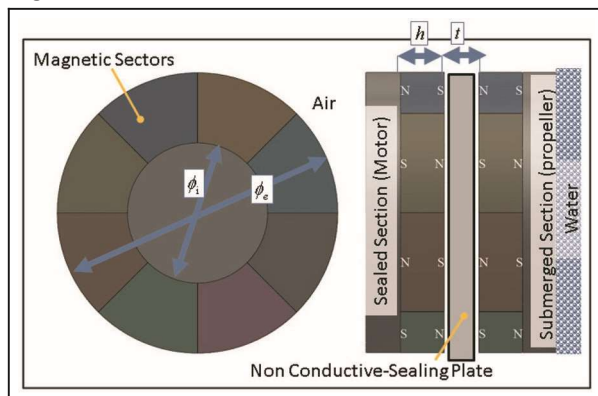
joint with a simplified geometry. Since a real joint has to be assembled from commercial components, whose geometry and features differ from the ideal case

proposed in the literature, further simulations were performed using FEM simulation tools and in particular COMSOL Multiphysics, as shown in Figure 18.

Commercial neodymium-bore magnets have often prismatic or cylindrical shapes, so the elementary magnets have to be assembled to produce the desired lay-

out. Using both MATLAB and FEM models, it was possible to evaluate the effects on the transmitted torque of some design parameters such as the air gap among the magnets and the number of the magnetic poles. The results shown in Figure 19 are calculated for an axial joint with internal and external diameters  $f_i$  and  $f_e$  of about 20 and 40 mm and a depth  $h$  of about 10 mm. The results of the analysis show that the design is very sensitive to the air gap, which may be variable considering the use of different construction materials for the walls of the sealed section or different specifications about the maximum operating depth. From this

Figure 16. Simplified scheme of a magnetic joint with axial flux design.



point of view, the design of a radial magnetic joint is

more robust against these parametric uncertainties compared to the axial one:

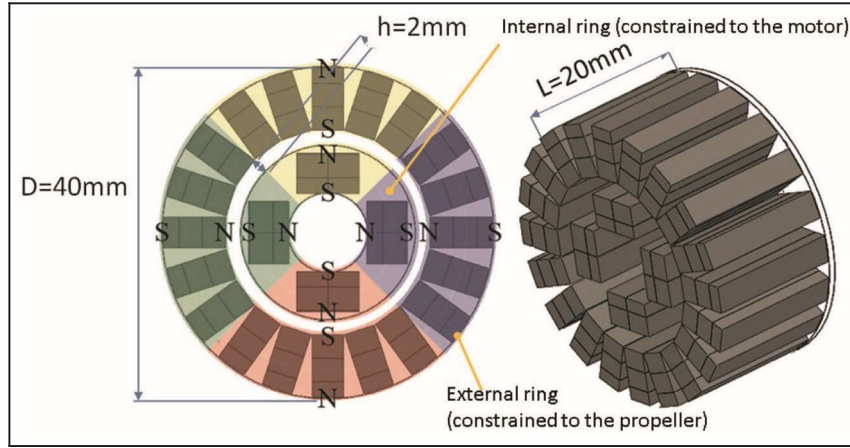


Figure 17. Simplified scheme of a magnetic joint with radial flux design. L value is referred to the version designed for the lateral thrusters.

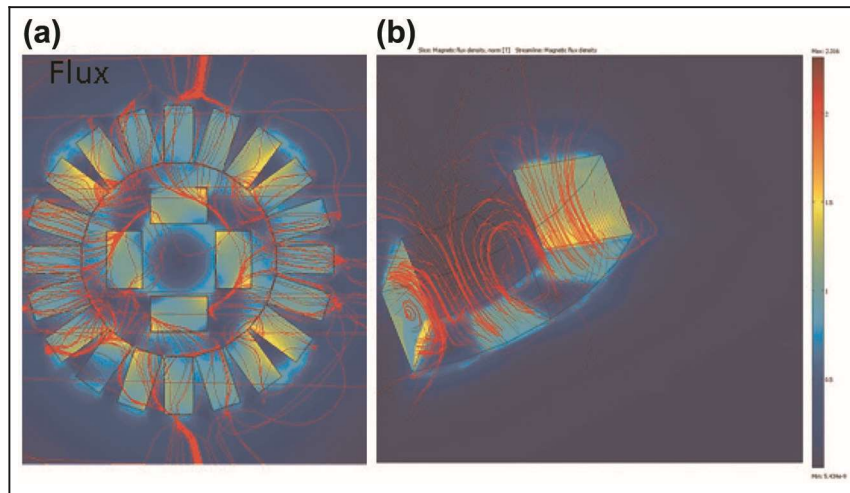


Figure 18. Magnetic flux density calculated by FEM models of magnetic joints with (a) radial and (b) axial flux.

Air gap design. The two parts of the joint are separated by a cylindrical air gap; from a structural point of view, building a cylinder shell able to resist to the water pressure, especially using composite or plastic materials, is easier. As a consequence, the value of the air gap is less sensitive to external pressure or to material properties;

Modularity. The transmitted torque is proportional to the total length of the joint L, as described in Figure 17. The value of the maximum delivered torque can be varied simply changing the value of L with limited effect on the mechanical and magnetic designs of the system;

Design and simulation. The magnetic circuit can be simulated using bi-dimensional models, which require limited computational resources.

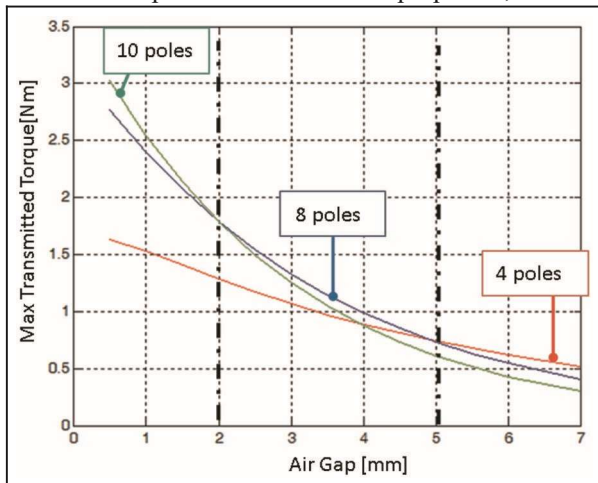


Figure 19. Maximum delivered torque for an axial joint as a function of the air gap (h) and the number of poles-polar expansion of the joint.

Both for the propellers and the thrusters, the authors designed a modular radial joint, as shown in Figure 17, whose length L is customized to fit different torque specifications for propeller and thruster actuators. A prototype of the proposed radial flux joint, as shown in Figure 20, has been assembled using a 3D printer for plastic/non conductive components. This solution adopts four poles assembled using highperformance bore-neodymium magnets. Using the equipment described in Figure 20, it was possible to verify, with static tests, the



maximum torque transmissible by the joint, verifying calculations of the FEM model, as shown in Table 4. 3D FEMs slightly underestimate the transmissible torque; however, the error introduced is compatible with the

friction on bearing and to an overestimation of reluctance in the FEM model due to the discretization introduced by a rough mesh. The two-dimensional (2D) model errors are

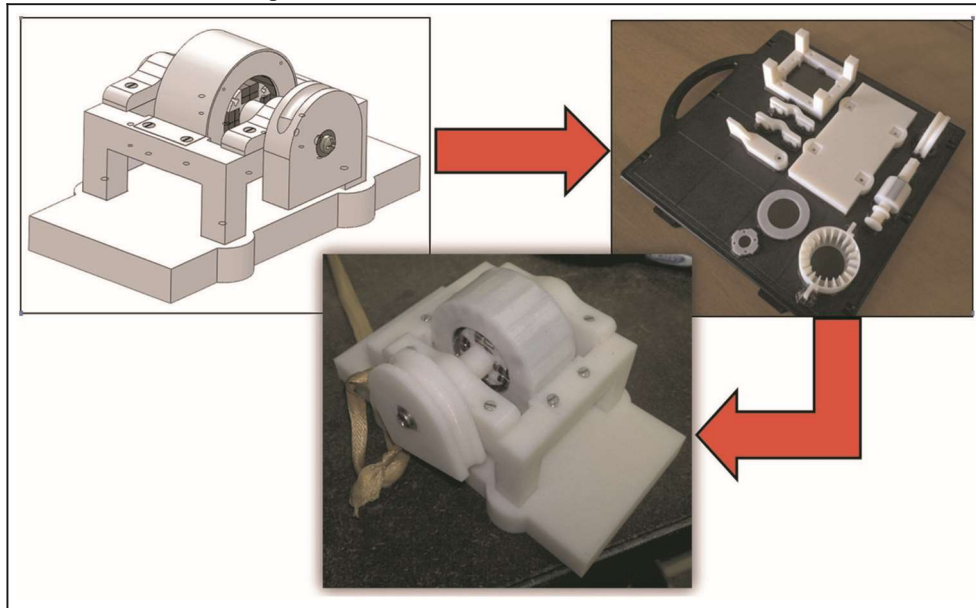


Figure 20. Fast prototyping of a radial magnetic joint, including equipment for static tests.

Table 4. Comparison between the maximum transmissible torque and FEM calculations.

Torque (% compared to experimental)	FEM 2D	FEM 3D	Experimental
	1.6 N m (220%)	1.85 N m (27.5%)	2.0 N m

FEM: finite element model; 2D: two-dimensional; 3D: three-dimensional.

Figure 21. Simplified FEM model of the sealed motor case filled with oil.

higher and are mainly due to the boundary effects, which are quite important considering the  $L=D$  ratio of the simulated joint of about 0.5. For longer joints ( $L=D \gg 1$ ), the relative error on 2D FEM computation is much lower because the importance of the boundary effects decreases. Finally, it is worth noting that the properties of the adopted magnetic materials are affected by tolerances and uncertainties of about 5%–210%.

### Design of the oil-filled actuator

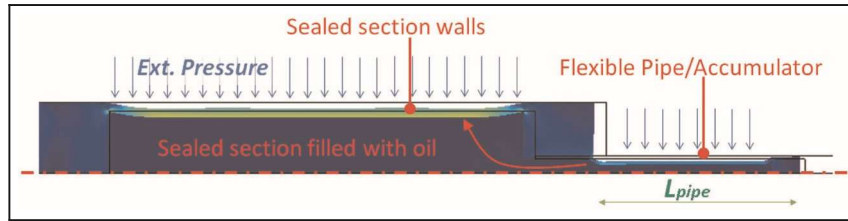
As previously introduced, considering oil-filled actuators, the external pressure of water has to be compensated by the hydrostatic pressure of the oil, which is used to fill every air gap inside the sealed section. Since the actuator is closed with a cylindrical thin wall case, the difference between the internal pressure of oil  $P_{oil}$  and the external pressure of surrounding water  $P$  can be easily calculated according to equation (16), in the simplified hypothesis of assuming a constant bulk modulus  $E_{oil}$  for the internal volume of a sealed case with radius  $r$  and lateral walls with known thickness  $t$  and Young modulus  $E$

$$\frac{2\delta P_{oil} P r}{\delta 16 P t E E_{oil}} = \frac{P_{oil}}{P} = \frac{2r E_{oil}}{(tE + 2r E_{oil})}$$

On the other hand, maximum stress  $s_{eq}$ , the lateral case walls are subjected to, is proportional to the  $r=t$  ratio, as stated by equation (17)

$$s_{eq} = \frac{r}{t} \frac{P_{oil} - P}{E} = \frac{r}{t} \frac{P}{E} \frac{2r E_{oil}}{(tE + 2r E_{oil})}$$

Considering both relations (equations (16) and (17)), the case construction can be optimized in two ways:



The use of materials with high tensile strength and low Young's modulus reduces the stress induced by pressure;

A flexible wall or a membrane, with negligible stiffness, used to directly transmit external pressure  $P$  to the oil reduces the difference between  $P$  and  $P_{oil}$  and, consequently, the mechanical stress induced on the sealed case. In Figure 21, a simplified FEM model of the proposed solution is shown; it is worth noting that the compensating effect can be improved by simply increasing  $L_{pipe}$ , the length of the flexible pipe, or using a less stiff pipe.

A notebook running the driver diagnostic software. A notebook is linked through an emulated serial connection to the motor driver. Using the diagnostic software of the driver, it is possible to evaluate the behaviour of all the measured and estimated

Since the oil fills the motor windings, electric insulation and stability against thermal ageing have to be assured. Therefore, silicon or synthetic oil for transformers and power devices has to be used. A good reference to choose sealing and to verify chemical compatibility between different materials is provided by Brown.<sup>37</sup> From a thermal point of view, the presence of oil in the motor should produce an increase of viscous losses, reducing efficiency and consequently increasing the dissipated heat inside the motor as stated by Zou et al.<sup>38</sup> with negative consequences for very high rotation speed; however, the presence of a liquid inside the motor windings improves motor cooling with the surrounding water. Consequently, it is thus possible to overload the actuator of more than 130%, as stated by technical reports of brushless motor manufacturers.<sup>39-41</sup> It is also a common practice between producers of commercial low-cost marine actuators to overload motors for peak performances even to 200%2400% with respect to rated performances in air, exploiting cooling effect of both surrounding water and oil inside the motor.

## Preliminary testing activities

Both rear propellers and thrusters have been tested in a pool using the simple experimental equipment, as described in Figure 22:

Propeller prototype. Prototype of actuator to be tested;

Thrust measurement. A load cell is used to measure the thrust;

Guides. Prismatic guides are used to compensate the reaction torque of the propeller;

Controlled power device. A controlled source of electrical power and other instruments are used to supply the tested actuator and to measure the power consumption;

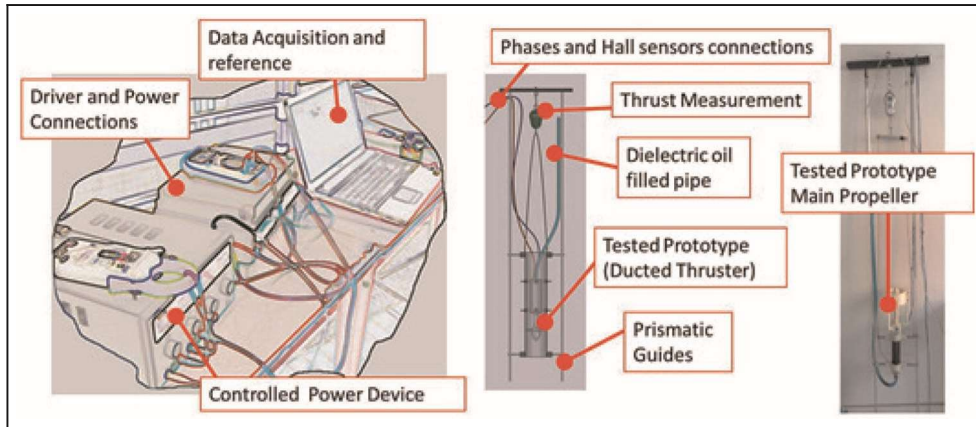


Figure 22. Experimental layout used to verify the actuator performances.

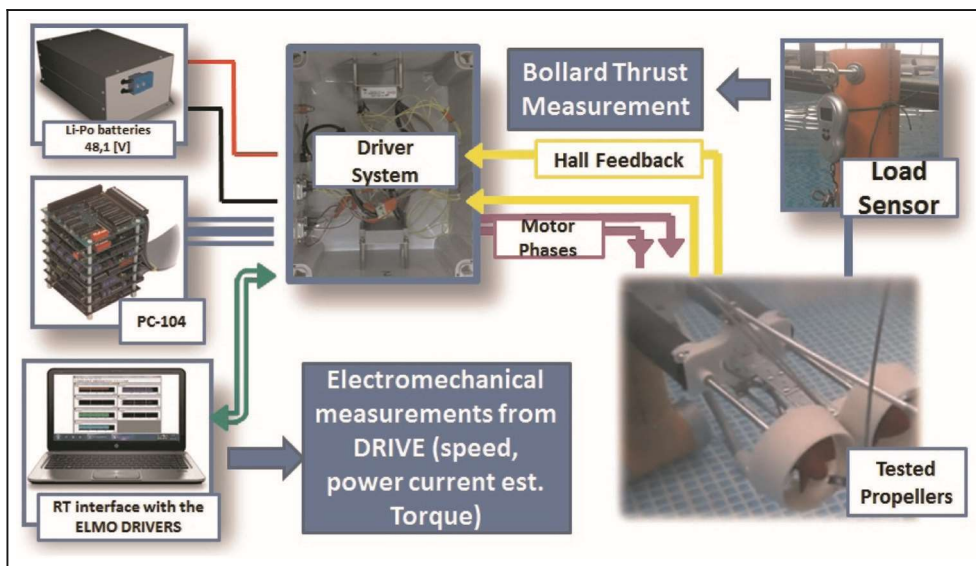


Figure 23. Experimental layout used to verify the actuator performances of coupled rear propellers.

RT: real-time.

electromechanical state variables such as currents, voltages, estimated electrical torque and so on.

Similar testing layouts have also been used for the preliminary testing of coupled rear propellers and of through-body thrusters, as shown in Figures 23 and 24.

### Preliminary testing results

Using the testing devices described in Figures 22 and 24, it was possible to experimentally evaluate the bollard thrust delivered by the propellers as a function of rotating speed and needed electric power with different  $p=d$  ratios. The results are resumed in Figure 25: propeller profiles with  $p=d=1:2$  and  $p=d=1:4$  are the most efficient ones, but the profile with  $p=d=1:4$  is also able to reach the highest thrust for the same speed. Further optimization involves a more accurate knowledge of the hydrodynamic resistances of the vehicle, which are only estimated through FEM calculations. From

the experimental results, it was possible to identify the value of thrust and torque coefficient,  $K_t(0)$  and  $K_q(0)$ , for a null value of the advance coefficient  $J$  and to calibrate and validate  $K_t(J)$  and  $K_q(J)$  curves used for the design of the propulsion system.

The same tests have been performed for the lateral and vertical thrusters, and the corresponding results are displayed in Figure 26:

The efficiency is generally much lower, compared to the rear propellers; in particular, high losses are introduced by the protection grids, which have been placed at the end of the thruster tunnel (a nylon net with 6 3 6 mm quadrangular holes). The protection grids have been inserted to protect the ducted thrusters from biofouling. To have an idea of the losses, the authors have performed some tests removing the protection grid whose results are shown in Figure 27. The tests are performed with a  $p=d$  ratio equal to 1: since the losses are quite high (about

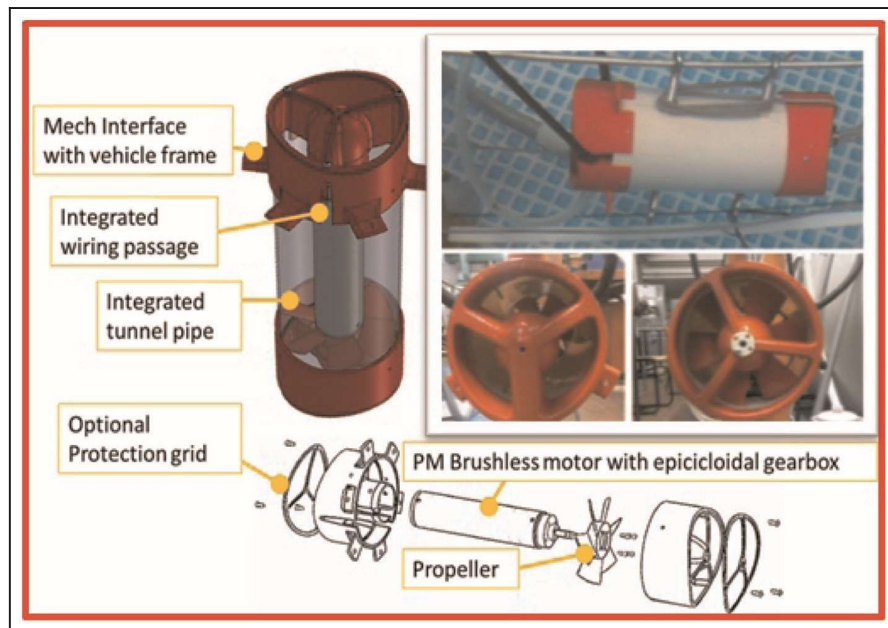


Figure 24. Through-body thruster, main components and testing devices.  
PM: permanent magnet.

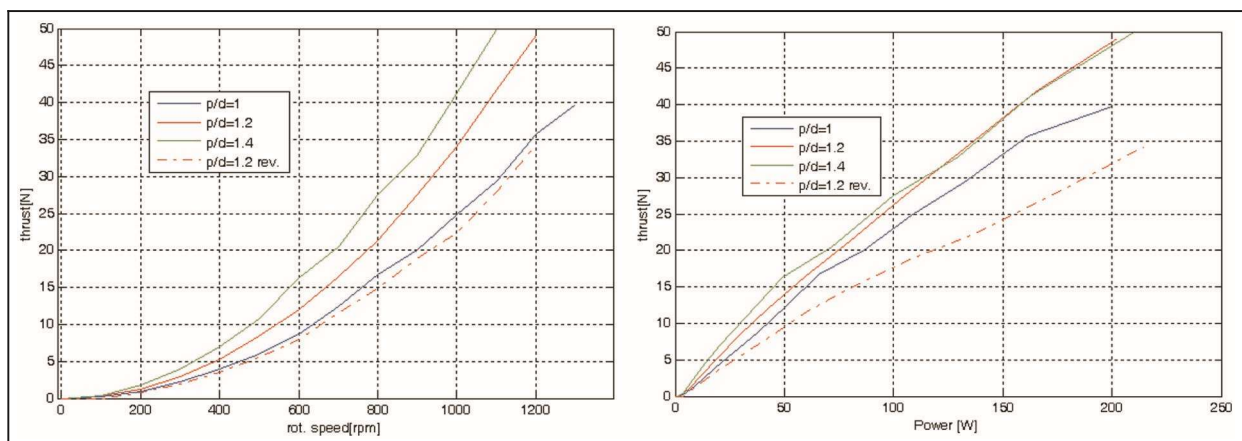


Figure 25. Testing of the propeller bollard thrust behaviour, considering forward rotating speed (continuous line) and the reverse one (dashed line).

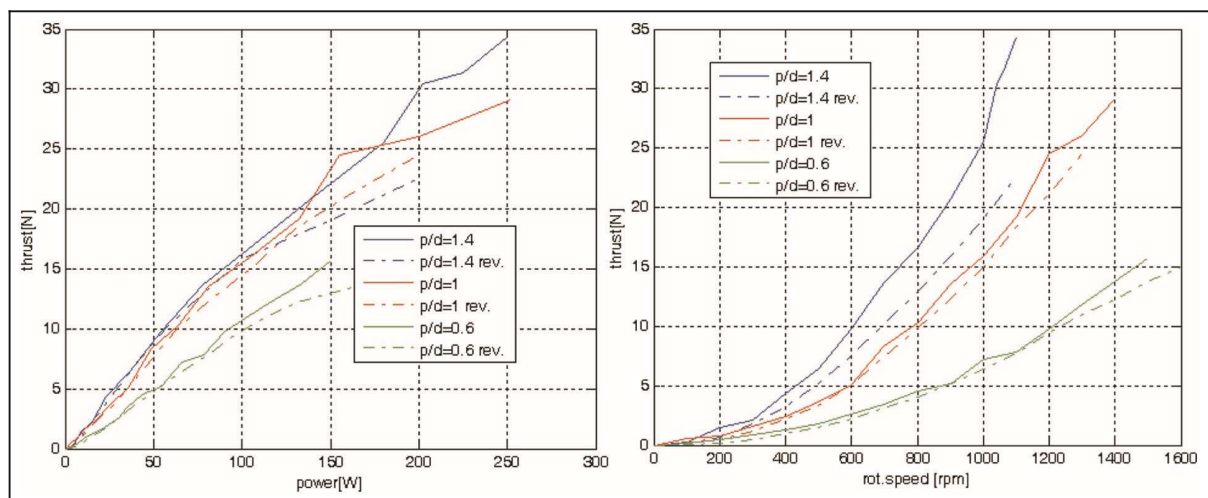




Figure 26. Testing of the bow thruster bollard thrust behaviour, considering forward rotating speed (continuous line) and the reverse one (dashed line).

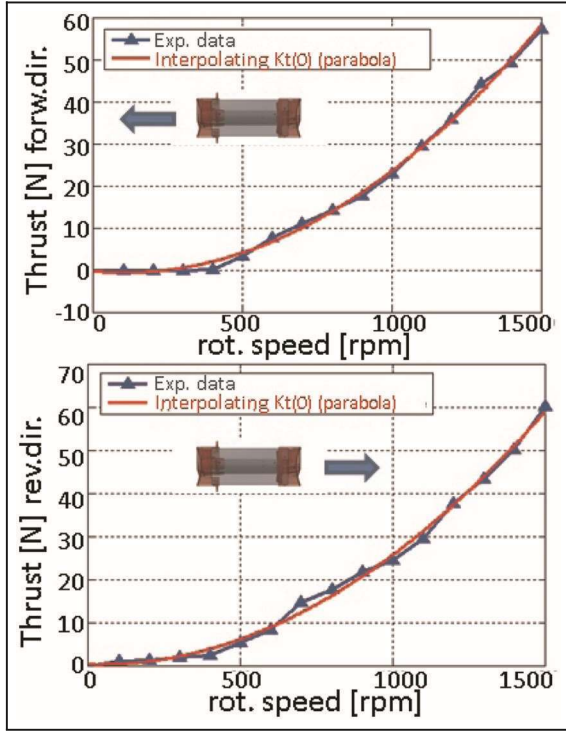


Figure 27. Testing of the bow thruster bollard thrust behaviour for both directions with no protection grids ( $p=d=1$ ).

40%), the authors have decided to use protection grids only for particular mission scenarios;

Even adopting a symmetric profile for the thruster blades, the performances depend on the sign of the inlet flow since, for encumbrance reasons, the propeller is not centred into the tunnel length. Propellers with low  $p=d$  ratio are less sensitive to the sign of the advance speed.

Finally, for both propellers and thrusters, it was possible to verify the functionality of the actuators filled with dielectric oil: the presence of the oil inside the motor and the cooling effect increase the thermal capacity and the cooling coefficients of the actuator, which can be overloaded in terms of currents on the windings. The presence of the oil among the moving parts of the stator and the rotor increases viscous/mechanical losses especially at high rotating speeds (8000–10,000 r/min) where motor efficiency drastically decreases (from 85% to 75%); consequently, as shown in Figure 28, the performance improvement is more evident at lower rotating speeds where both induced voltages on coils and internal viscous losses are lower.

This is a very useful feature since the maximum power delivered by the motor is less sensitive to the speed of rotation, so it is possible also, for example, to use propeller with a higher  $p=d$  ratio. Considering the results of the experimental activities, the authors preferred to install for the rear propeller a direct drive brushless motor able to deliver

its nominal power directly at 2000–2500 r/min without any reduction

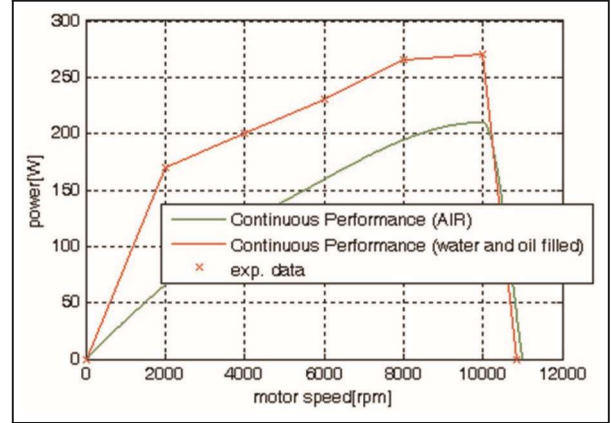


Figure 28. Rough estimation from experimental data of the continuous performance curve with respect to the cooling conditions.

stage. As a consequence, the weight of the motor was doubled but there was a further increase in efficiency since losses due to gearbox were eliminated and also the oil viscous effects were reduced considering that the peripheral rotor speed was about a half as the original motor. Power drive and electronics remain the same because the different choices of the motor winding configuration (triangle/star) and poles were exploited to keep the values of absorbed current almost constant compared to the previously chosen solution.

### Calibration of a simplified actuator model

The preliminary simulations of the vehicle behaviour involve the availability of a nearly realistic model of the actuation system that has to be calibrated using experimental data or simulation results according to the project state. Following a common approach,<sup>42</sup> the dynamic behaviour of the thruster can be modelled according to equations (18) and (19), which represent the corresponding thruster model in terms of propulsion thrust  $T$  and propeller speed  $v$  (rad/s).  $\dot{v}$  is the time derivative of the propeller speed

$$T = \frac{K_t(J) r d^4}{4p} \dot{v}^2 = C_t(J) v \quad (18)$$

$$\frac{Q v^2 K_q(J) d^5 r}{2} \dot{v} = 2 I_{eq} = a Q C_q(J) v \quad (19)$$

where  $I_{eq}$  represents an equivalent reduced inertia taking into account both the contribution of the mechanical inertia of the actuator,  $I_{mech}$ , and of the dragged fluid flow,  $I_w$ ; in order to simplify equation handling, constant terms are condensed in  $C_t$ ,  $C_q$  and  $a$ .

Equations (18) and (19) are written neglecting the contribution of crossflows as modelled for instance by Palmer et al.<sup>26</sup>

For the main rear propellers, the crossflow effects could be neglected since they are oriented in the main motion direction of the vehicle so statistically the effects of crossflow are less important. For through-body tunnel thrusters, these effects as stated by Palmer et al.<sup>26</sup> depend on the squared rate between the outlet propeller speed and the mean speed of the impacting crossflow; as a consequence, this contribution is usually negligible only when the vehicle is performing hovering or very low-speed manoeuvring. Also the models suggested by Palmer et al.<sup>26</sup> have to be calibrated, considering interactions with the hull. The authors preferred to neglect these terms in the preliminary modelling of the vehicle and to further refine the model when more experimental data concerning missions and identification tests of the vehicle should be available.

The above-mentioned equations, the propeller interaction with the inlet flow is modelled since both  $C_t(J)$  and  $C_q(J)$  coefficients are modelled as a function of the advance coefficient  $J$  and so of the relative speed of the advance speed  $V_a$ , introducing also the effect of current disturbances:<sup>12</sup> in a model of the vehicle dynamics, the effect of the coupling between the propeller and the hull can be evaluated. It should be noticed that in many specialized studies available in bibliography,<sup>12</sup> the dynamic behaviour of the motor and power electronics in terms of transfer functions between the reference command and corresponding torque  $Q$  given by the motor to the propellers is also modelled. The authors deliberately neglected this contribution since the measured response times and dynamics of the chosen motors and drives are too fast compared to the vehicle ones.

On the other hand, considering the main features of modern power drives used to control brushless motors, two different control schemes, which imply two different modelling approaches, should be considered:

**Current–torque-controlled scheme.** On permanent magnet brushless motors, delivered torque  $Q$  is roughly proportional to the current. As a consequence, if the electronic drive is configured for current control, it should be assumed that the system is modelled as a simple current reference, saturated according to motor performances, which is used to directly calculate the actuator dynamics from equations (18) and (19). This approach is most often followed since it can be easily implemented and understood from a physical point of view. The main drawbacks of this procedure are hidden in the calculation or in the estimation of coefficients  $a$ ,  $C_t(J)$  and  $C_q(J)$ , which are often affected by heavy uncertainties. A sensitivity to uncertainties,

concerning friction torques derived from sealing, efficiency of mechanical transmission and internal viscous losses (especially for oil-filled systems) should be considered. The modelling of these nonlinear effects should be difficult considering the construction tolerances of motors and further uncertainties, since friction and viscous effects are influenced by wear and thermal effects;

**Speed-controlled scheme.** The propeller speed is directly controlled by the actuator. For a wellcalibrated and sized system, it should be considered

a null or negligible error between the reference speed command of the drive and the measured feedback one of the motor and propeller. There are two main advantages of speed-controlled drives:

**Friction and disturbance rejection.** Since the motor is speed controlled, internal friction and other spurious torque disturbances, which could affect torque-controlled drive, are rejected by the action of the closed-loop speed control;

**Open-loop control of the vehicle speed.** For the main rear propellers, there is a nearly proportional relationship between the rotational speed of the propellers and the steady-state value of the vehicle one when performing a straight trajectory. This relationship may be approximately calculated knowing the vehicle drag coefficients or the tabulating experimental data.

For the application on Tifone vehicles, drives and motors of both rear propellers and tunnel thrusters are configured to be speed controlled.

## Calibration and identification of speed-controlled drives

As previously introduced, on Tifone vehicle, the propeller speed is directly controlled by the motor drive. The response of the motor drive has to be calibrated and identified with experimental tests, which are performed using the same experimental devices described in Figures 22–24.

In order to better identify the system performance, the closed-loop speed of the drive is implemented as a simple high-gain proportional controller described by equation (20) where  $Q_{ref}$  represents the torque current reference for the drive system, which is proportional, with a factor  $K_p$ , to the error between the reference speed and the measured one. All the tests are performed in static conditions (null advance speed, bollard thrust,  $J=0$ ) considering different step amplitudes whose test parameters and results are shown in Table 5 and Figures 29 and 30

$$Q_{ref} = K_p (v_{ref} - v) \quad \delta 20p$$

From the analysis of the experimental tests, the following considerations are taken into account:

The dynamical behaviour of the actuated propeller is very fast considering the desired behaviour of the vehicle. Measured rise times and angular accelerations are probably underestimated considering the sampling frequency of the data imposed by the internal diagnostic of the drive system;

Propellers are subjected to heavy angular accelerations corresponding to  $10^2$   $10^3$   $\text{rad/s}^2$  or even more considering the low sampling frequency used. These values are quite high, so the maximum propeller acceleration should be limited in order to

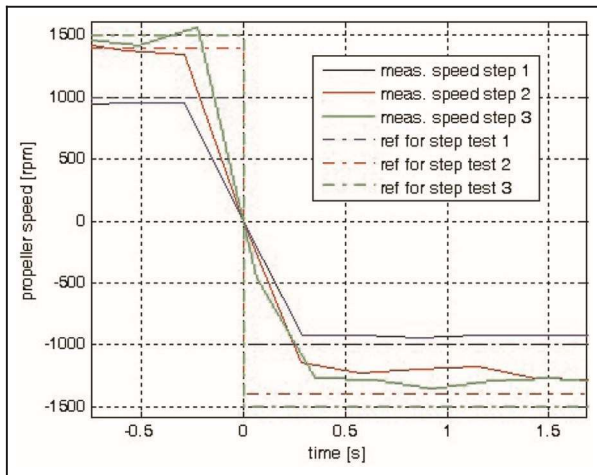


Table 5. Step test on propellers.

Test number	Initial speed (r/min)	Final speed (r/min)	Sample time (s)	Rise time (s)	Mean ( $\text{rad/s}^2$ )	deceleration
1	1000	21000	0.288	0.6	350	
2	1400	21400	0.288	0.6	480	
3	1500	21500	0.288	0.7	445	
4	0	1000	0.144	0.15	600	
5	0	1500	0.144	0.15	900	

Figure 29. Results of step tests 1–3 (sampling/acquisition frequency of 0.288 ms).

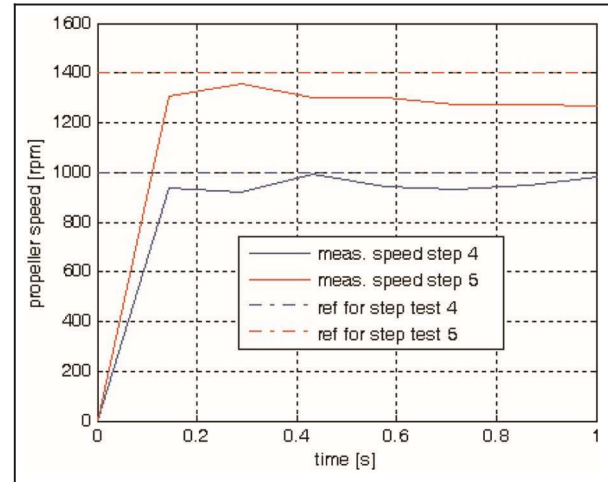
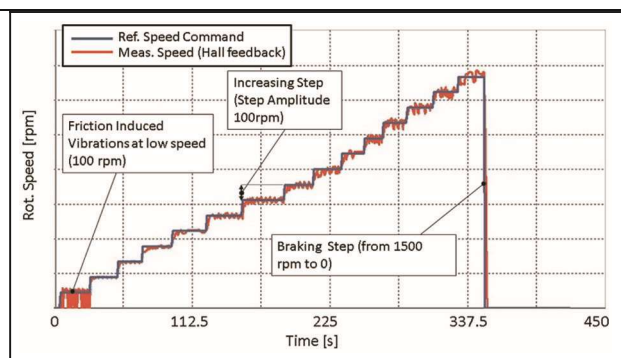


Figure 30. Results of step tests 4 and 5 (sampling/acquisition frequency of 0.144 ms).

preserve the structural integrity of the mechanical components. However, if no acceleration limitation is introduced, the transient associated with the propellers and thruster is so fast that can be neglected;

The dynamical behaviour described by equation (19) is rejected by the speed loop controller, exploiting the overload capability of the actuator for intermittent



loading conditions;

Since the tested regulator is a simple proportional controller with a constant gain, a static error as to the reference speed is clearly recognizable; the static error

Figure 31. Smooth response for a multiple-step test of the gain-scheduled controller.

is proportional to the resisting torque and consequently to the squared value of speed. A gainscheduled proportional–integral regulator has

been implemented to improve the control performances reducing to 0, the steady-state error on regulated speed. In particular, in Figure 31, some experimental results (bollard tests in pool) concerning the gainscheduled regulator are shown: it is clearly noticeable that the chosen regulator is able to regulate in a very precise way the speed of the propeller for speed higher than 100 r/min. In fact, for very low rotation, the speed thrust and torque of the propeller are negligible and the dynamical behaviour of the motor is dominated by internal viscous and friction phenomena.

### Preliminary extrapolation of main propeller performances from bollard thrust tests

Using the simplified testing layout described in Figures 22–24, only static test corresponding to a null advance coefficient ( $J=0$ ) can be carried out. In order to assemble a Simulink propeller model that will be integrated into a complete vehicle model, as the one described by Fossen,<sup>12</sup> a  $T(V_a, v)$  function for nonnull values of advance coefficients has to be extrapolated. The profiles used for the main rear propellers derive from  $K_a$  profiles. From the literature,<sup>28–30</sup> the performances of ducted  $K_a$  propellers are known. From experimental bollard thrust tests, the authors have been able to identify the values of both thrust ( $K_t(0)$ ) and torque ( $K_q(0)$ ) coefficients for a null advance value ( $J=0$ ). Introducing a constant scaling factor, defined as the ratio between the measured bollard thrust coefficient and the tabulated one from the literature, the

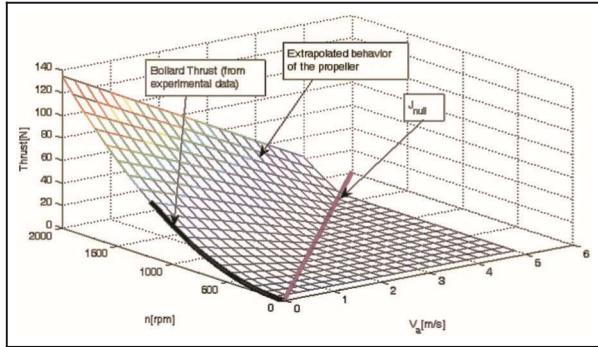


Figure 32. Extrapolated behaviour of main rear propellers (first quadrant).

authors extrapolate the behaviour of the rear propellers obtaining a surface whose shape for the first quadrant is shown in Figure 32 where the corresponding behaviour of thrust  $T(n, V_a)$  as to the rotation speed measured in revolutions per minute (rpm)  $n_{rpm}$  and the advance speed  $V_a$  are shown.

For through-body tunnel thrusters, due to lack of reliable data from the literature, the authors preferred to extrapolate the behaviour of  $K_t(J)$  and  $K_q(J)$  using a model based on a procedure in which the performance of the propeller is calculated imposing the conservation of

rothalpy as defined by Manfrida and Stecco<sup>43</sup> over several cylindrical sections of the propeller. Using this procedure, which is often adopted for preliminary rough calculations on axial flow turbomachinery, the authors were able to obtain  $T(n, V_a)$  that should be considered a nearly realistic solution for motions with null or negligible crossflows.

### Preliminary simulations of vehicle performances and autonomy

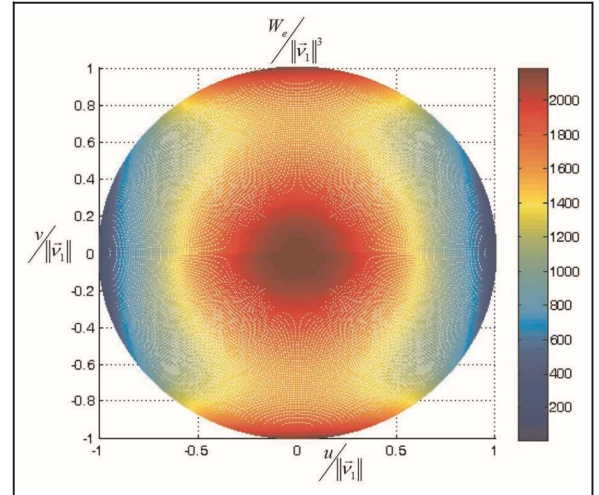
In order to simulate the dynamical response of the AUV, a MATLAB/Simulink model of the vehicle has been developed and used also for a first calibration of navigation and localization algorithms<sup>44,45</sup> following the approach proposed by Fossen,<sup>12</sup> which is described by equation (21)

$$M\ddot{n} + C\dot{\delta} \dot{n} + D\ddot{\delta} \dot{n} + \ddot{g} \dot{n} = \ddot{t} \quad \delta 21b$$

where vectors  $\ddot{t}$ ,  $\ddot{n}$  and  $\ddot{h}$  are defined according to Table 1.

Matrices  $M$ ,  $C$  and  $D$  are introduced to model the contributions of the inertial, Coriolis and viscous effects, as defined by Fossen.<sup>12</sup> Vector  $\ddot{g}$  represents the combined effects of gravity and buoyancy. Knowing the thruster configuration, the relation between the propeller forces and corresponding  $\ddot{t}$  exerted on the vehicle can be easily computed.

Implementing both the vehicle and thruster submodels in a single Simulink model, it is possible to calculate the efficiency of the vehicle in terms of ratio between needed



electrical power  $W_e$  and the cubic value of the module of the vehicle linear speed  $k^3 n^3$ . This

Figure 33. Simulated power consumption over cubic advance speed ( $W s^3=m^3$ ) for vehicle pure translation motions in different directions.

calculation is performed combining longitudinal, lateral and vertical motions of the vehicle considering steady state conditions assuming the following conditions are valid:



$p=q=r=0$ : It is a pure translation motion; no rotation occurs ( $\tilde{k} = k$ );

$\tilde{k}^2 = u^2 + v^2 + w^2$ : The velocity of the vehicle is the sum of its three scalar components;

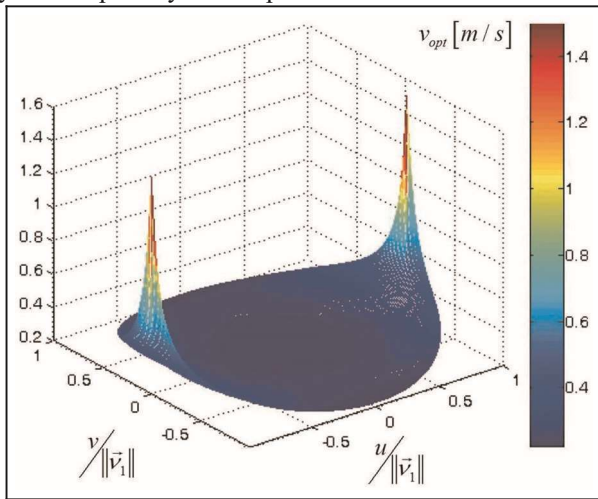
Crossflow effects on thruster performances are neglected (this assumption involves that the reliability of the calculation is much higher for motions whose directions are perfectly aligned with one of the three reference directions  $x-z$ ).

This way the ratio  $W_e = \tilde{k}^3$  is defined as a function  $u, v, w$  and consequently of the direction of motion. Some preliminary results are shown in Figure 33. As clearly shown in Figure 33, pure lateral and vertical translations are extremely inefficient with respect to the advance in longitudinal direction.

Value of  $W_e = \tilde{k}^3$  is also an index of the propulsion system capability to keep the vehicle stable in hovering

against a water current disturbance: considering the results of Figure 33, the vehicle is able to resist in hovering with affordable energy consumptions to a lateral current disturbance of about 1 knot. For a higher current disturbance and, more generally, for a higher speed, it is much more convenient to turn the vehicle to align its longitudinal axis to the desired direction of motion, also considering that the energy consumptions associated with the vehicle rotations are much lower: particularly, assuming a pure rotation along the body pitch and yaw axis ( $u=v=w=0$ ), the two power ratios  $W_e = q^3$  and  $W_e = r^3$ , calculated for steady-state conditions, are equal to about 250 and 140 ( $W \cdot s^3$ ), respectively, which implies a good handling and manoeuvring of the vehicle. It is worth noting that

Figure 34. Calculation of  $V_{opt}$  considering a value of  $W_{inst}$  equal to 50 W.



previous calculations are performed considering the penalized performances of the thrusters covered by protection grids in order to protect them from excessive biofouling.

The energy consumption is very sensitive to the advance speed and travelling direction. For the optimization of the vehicle autonomy and efficiency, it is important to approximately evaluate a value of the translation speed  $n_{opt}$ , which minimizes the energy consumption considering the travelled distance  $s$  in the simplifying hypothesis of pure translation motion. The total power needed by the vehicle  $W_{tot}$  can be calculated summing two terms:  $W_e$  power needed for propulsion and  $W_{inst}$  the power needed by on-board subsystem including the vehicle logic, sensor payload and instrumentation (equation (22))

$$W_{tot} = f \left( \frac{u}{\tilde{k}}, \frac{v}{\tilde{k}}, \frac{w}{\tilde{k}} \right), \quad \tilde{k}^3 + W_{inst}$$

The value of  $W_{inst}$  is variable according to the mission profile and the energy consumption of on-board subsystem. The

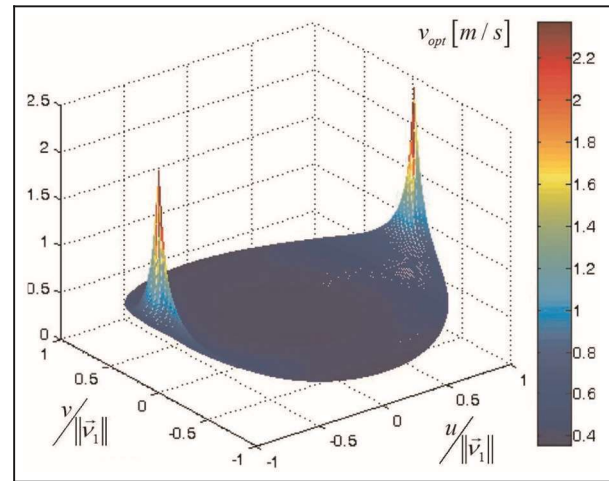


Figure 35. Calculation of  $V_{opt}$  considering a value of  $W_{inst}$  equal to 200 W.

value of  $W_e$  depends on both the module and the directions of the travelling speed  $\tilde{n}_1$ .

As a consequence, it is possible to optimize the vehicle speed to maximize some parameters of interest such as the vehicle autonomy during the motion as to a known straight direction. In particular, considering a pure translation motion at constant speed, the corresponding  $n_{opt}$  can be calculated as a function of the travelling direction according to the following equation

$$n_{opt} = \sqrt[3]{\frac{W_{inst}}{\tilde{k}^3}}$$

The  $n_{opt}$  as a function of  $u, v, w$  functions, calculated for  $W_{inst}$  values of 50 and 200 W, are shown in Figures 34 and 35, respectively: the value of  $W_{inst}$  does not influence the

optimal travelling direction, which remains obviously the longitudinal one. However, it is interesting to note that a low energy consumption of on-board subsystem implies a lower value of the vehicle optimal speed and consequently a higher autonomy, showing that the optimization of the vehicle efficiency can be managed considering the whole vehicle, including all on-board subsystems, and not only the propulsion one.

For the vehicle travelling at  $n_{opt}$ , it is approximately verified a linear relationship between the electrical power needed for propulsion and on-board subsystem (equation (24))

$$\frac{W_e}{2} = \frac{W_{inst}}{3} + \frac{W_{tot}}{3} \quad (24)$$

It is interesting to note that the proposed relation (equation (24)) is nothing more than a 3D generalization of the scalar optimal speed calculation method proposed by Singh et al.<sup>46</sup> The obtained results are quite realistic considering the calculated optimal speed in the longitudinal direction has a value between 3 and 5 knot, which is quite realistic compared to the performances of many existing vehicles.

## Conclusion

In this study, the design and testing activities concerning AUV Tifone and its propulsion system have been presented. It is interesting to note that most of these activities, starting from the vehicle design to the testing and the assembly of three vehicles, have been performed in less than 18 months, with limited resources, mostly using self-designed and assembled components. This way, a key role for the development of the project was played by the integrated use of CAD, computeraided engineering (CAE) and fast prototyping tools, which make possible a rapid design and manufacturing of parts and high-performance components that can be easily found in the general-purpose market of automation. In particular, plastic materials used for fast prototyping, despite poor mechanical properties, are light, easy to be machined, less sensitive to corrosion compared to several metal alloys and able to resist to high pressures (depths). Fast prototyping could also give a fundamental contribution for the development of auxiliary parts or devices needed for the testing of the components (e.g. in the case of Tifone propellers or magnetic transmission systems) or to produce intermediate components, which are fundamental for manufacturing parts of the hull or to shape fibreglass sheet for a fast production of hull components. Considering the continuous improvements of fast prototyping technology and of surface treatments suitable to further improve mechanical properties, it could be a highly feasible extension of the use of this technology to the fast and cheap design of competitive and innovative

AUVs: this scenario could be particularly interesting for a small- and medium-sized research team who have more difficulties to access expensive infrastructure. Focusing on the aim of this study, the development of the vehicle propulsion system, the proposed hybrid solution has been designed as an open system that in the current configuration is a good trade-off between different missions and design specifications that could be further modified considering the modularity and flexibility of the chosen components: for instance, the electronic power drive is able to perform position, speed and torque control of a wide variety of motors and actuators. In particular, the choice of a unified size for motors (200 W) and propellers (120 mm), which drastically simplifies the design, testing and construction of the system, was made possible by the unconventional use of two rear main propellers, which are quite uncommon on torpedo-shaped AUVs. The authors would also point out that an integrated self-design of the propulsion system considering the electrical, mechanical and fluid dynamic behaviour is a good practice not only for the optimization of the propulsion, but also for the identification of the system, an accurate modelling and, more specifically, a better comprehension of the vehicle dynamic behaviour. Also in this case, the proposed design procedures have been trade-off solutions, which are quite innovative especially as regards the design and the testing of the magnetic transmission systems. Finally, in accordance with the aims of THESAURUS project, it was possible to build a highly customizable middle-sized vehicle with affordable costs and performances, which are comparable to much more expensive vehicles developed by consolidated research groups in terms of energy/weight ratio, speed and autonomy, and use of composite non-metallic materials. Cost, time to market and easy customization are fundamental prerequisites to extend the use of coordinated swarm of middle-sized vehicles to cost-limited applications. Currently, THESAURUS vehicles are completely assembled and are performing their first navigation missions, which are necessary to calibrate on-board navigation software and to test swarm



Figure 36. Preliminary testing activities in Roffia Lake (spring 2013): ROV mode and AUV mode.



Figure 37. Testing activities in the Ligurian Sea (summer 2013): AUV mode.

coordination and localization algorithms, which will be the objects of future publications. In particular, in Figures 36 and 37, there are some images referred to preliminary navigation testing in Roffia Lake (San Miniato, Pisa, Italy) and Ligurian Sea (La Spezia, Italy).

As clearly shown in Figures 36 and 37, the double rear propellers are covered by 5–10 cm of water when the vehicle travels in surface, so their functionality is degraded but not so compromised as in the case of a single bigger rear propeller. Also, an adjustment of the vehicle pitch angle and an optimal choice of the rotation sense of rear propellers should contribute to assure a more stable behaviour of the vehicle when travelling on surface. A further advantage of this solution is that in-surface GPS and communication antennas are further elevated and protected with respect to water surface.

### Further developments

For the mere design of the propulsion system of Tifone, the authors are planning some accurate identification tests of the hull vehicle in order to further verify and optimize the design of the system. When this activity is completed, the authors will be able to evaluate some mis-modelled contributions, such as the crossflow effects on thrusters, which are currently neglected or roughly approximated; moreover, the propellers and thrusters should be further optimized and ready to be manufactured in their definitive versions. The same drive system and wiring could be used to implement a position control of a rudder or navigation/control surfaces. More generally, the authors are designing smaller sized AUVs, for European projects such as ARchaeological ROBot systems for the World's Seas (ARROWS)), which will be assembled in the next months. Consequently, the authors are also working on smart criteria to further simplify and accelerate the design and the optimization of the propulsion system, taking into account

also the possibility of less conventional (such as internal ring motors) or bio-inspired propulsion methods.

### Acknowledgements

The authors express their gratitude to the engineering consultants and students, for their passion and their ideas: in particular, Marco Natalini, Marco Montagni, Marco Pagliai and Agostino Stilli. Finally, the authors wish to thank all the partners of THESAURUS project and in particular Professor Andrea Caiti (THESAURUS project Coordinator, University of Pisa, Italy), Lavinio Gualdesi and Michele Cocco ([www.edgelab.eu](http://www.edgelab.eu)) whose consolidated experience in marine engineering was an indispensable support for the project.

### Declaration of conflicting interests

The authors declare that there is no conflict of interest.

### Funding

This study was supported by Regione Toscana, who funded the THESAURUS project, I.T.T.S. Fedi-Fermi Provincia di Pistoia and secondary school (Pistoia) and Chino Chini (Borgo San Lorenzo), which indirectly supported these activities, cooperating with the MDM Lab of the University of Florence. Fundamental support was also provided by Center for Maritime Research and Experimentation (CMRE) of La Spezia and in particular by Stefano Biagini, giving access to their pressurized chambers for the testing of the vehicles and the components.

### References

1. Saunders A and Nahon M. The effect of forward vehicle velocity on through-body AUV tunnel thruster performance. In: Proceedings of the OCEANS '02 MTS/IEEE, 29–31 October 2002, vol. 1, pp.250–259. Biloxi, Mississippi.
2. Curtis, T.L. ; Perrault, D. ; Williams, C. ; Bose, N. “CSCOUT: a general-purpose AUV for systems research,” Proceedings of the 2000 International Symposium on Underwater Technology, 2000. UT 00, Publication Year: 2000, Page(s): 73–77.
3. Stokey RP, Roup A, von Alt C, et al. Development of the REMUS 600 autonomous underwater vehicle. In: Proceedings of MTS/IEEE OCEANS, 2005, Washington, DC, 17–23 September 2005, vol. 2, pp.1301–1304. New York: IEEE.
4. Allotta B, Pugi L, Costanzi R, et al. Localization algorithm for a fleet of three AUVs by INS, DVL and range measurements. In: Proceedings of the 15th international conference on advanced robotics, 2011, Tallinn, 20–23 June 2011, pp.631–636. New York: IEEE.
5. Alvarez A, Bertram V and Gualdesi L. Hull hydrodynamic optimization of autonomous underwater vehicles operating at snorkeling depth. Ocean Eng 2009; 36: 105– 112.
6. Yu X and Su Y. Hydrodynamic performance calculation on mini-automatic underwater vehicle. In: Proceedings of the 2010 IEEE international conference on information and automation, Harbin, China, 20–23 June 2010, pp.1319–1324. New York: IEEE.



7. Jagadeesh P, Murali K and Idichandy VG. Experimental investigation of hydrodynamic force coefficients over AUV hull form. *Ocean Eng* 2009; 36: 113–118.
8. Ostafichuck PM. AUV hydrodynamics and modelling for improved control. PhD Thesis, The University of British Columbia, Vancouver, BC, Canada, 1997.
9. Hafmynd – Gavia Ltd. Gavia, <http://www.gavia.is/> (accessed 25 December 2010).
10. McPhail S. Autosub6000: a deep diving long range AUV. *J Bionic Eng* 2009; 6(1): 55–62.
11. Caffaz A, Caiti A, Casalino G, et al. The hybrid glider/AUV Folaga. *IEEE Robot Autom Mag* 2010; 17(1): 31–44.
12. Fossen TI. *Guidance and control of ocean vehicles*. 1st ed. Chichester: John Wiley & Sons, 1994.
13. Stevenson P, Furlong M and Dormer D. AUV shapes – combining the practical and hydrodynamic considerations. In: *Proceedings of the OCEANS 2007 2 Europe*, Aberdeen, 18–21 June 2007, pp.1–6. New York: IEEE.
14. Joubert P. Some aspects of submarine design part 1. Hydrodynamics (U). DISTRIBUTION STATEMENT A, Approved for Public Release Distribution Unlimited (20041130), DSTO-TR-1622, October 2004. Fishermans Bend, VIC, Australia: DSTO Platforms Sciences Laboratory, Commonwealth of Australia.
15. Daniel RJ. Considerations influencing submarine design. In: *Proceedings of international symposium on naval submarines*, The Royal Institution of Naval Architects, London, 1983, paper 1.
16. Phillips AB, Turnock SR and Furlong M. The use of computational fluid dynamics to aid cost-effective hydrodynamic design of autonomous underwater vehicles. *Proc IMechE, Part M: J Engineering for the Maritime Environment* 2010; 224: 239–254.
17. Phillips AB, Turnock SR and Furlong M. Comparison of CFD simulations and in-service data for the self propelled performance of an autonomous underwater vehicle. In: *Proceedings of the 27th symposium of naval hydrodynamics*, Seoul, South Korea, 5–10 October 2008, 15 pp. Seoul, South Korea: Office of Naval Research, <http://eprints.soton.ac.uk/63499/1/PhillipsABV3.pdf>
18. Byron J and Tyce R. Designing a vertical/horizontal AUV for deep ocean sampling. In: *Proceedings of OCEANS 2007*, Vancouver, BC, Canada, 29 September–4 October 2007, pp.1–10. New York: IEEE.
19. Phillips AB, Blake JIR, Boyd SW, et al. Nature in engineering for monitoring the oceans (NEMO): an isopycnal soft bodied approach for deep diving autonomous underwater vehicles. In: *Proceedings of 2012 IEEE/OES autonomous underwater vehicles (AUV)*, Southampton, 24–27 September 2012, pp.1–8. Piscataway, NJ: IEEE.
20. Griffiths G, Jamieson J, Mitchell S, et al. Energy storage for long endurance AUVs. In: *Advances in technology for underwater vehicles, conference proceedings*, 16–17 March 2004, pp.8–16. 16–17 March 2004, London: Institute of Marine Engineering, Science & Technology.
21. Sherman J, Davis R, Owens WB, et al. The autonomous underwater glider ‘Spray’. *IEEE J Oceanic Eng* 2001; 26(4): 437–446.
22. Ehsani M, Gao Y and Emadi A. *Modern electric, hybrid electric, and fuel cell vehicles: fundamentals, theory, and design*. Boca Raton, FL: CRC Press, 2009.
23. Thomas R, Bose N and Williams CD. Propulsive performance of the autonomous underwater vehicle ‘CSCOUT’. In: *Proceedings OCEANS 2003*, San Diego, CA, 22–26 September 2003, vol. 4, pp.2170–2183. New York: IEEE.
24. Steenson LV, Phillips AB, Furlong M, et al. Maneuvering of an over-actuated autonomous underwater vehicle using both through-body tunnel thrusters and control surfaces. In: *Proceedings of the 17th international undersea untethered submersible technology conference, Autonomous Underwater Vehicles Applications Center*, Lee, NH, 2011. 21–24 August 2011, Portsmouth, New Hampshire, USA.
25. Technical documentation on the Codevintec Seastick AUV, <http://www.codevintec.com>
26. Palmer A, Hearn GE and Stevenson P. Experimental testing of an autonomous underwater vehicle with tunnel thrusters. *Proceedings of the First International Symposium on Marine Propulsors - smp’09*, 22–24 June 2009, Trondheim, Norway. Edited by: Kourosh Koushan and Sverre Steen. In: *SMP’09 2 first international symposium on marine propulsors*, Trondheim, 2009, 6 pp.
27. Steenson L, Phillips A, Rogers E, et al. The performance of vertical tunnel thrusters on an autonomous underwater vehicle operating near the free surface in waves. In: *Proceedings of the second international symposium on marine propulsors, Proceedings of the Second International Symposium on Marine Propulsors - smp’11*, 15–17 June 2011, Hamburg, Germany. Edited by: Moustafa Abdel-Maksoud. Hamburg University of Technology, Hamburg, 2011.
28. Carlton J. *Marine propellers and propulsion*. 2nd ed. Elsevier, 2007.
29. Oosterveld MWC. *Wake adapted ducted propellers*. Wageningen: Netherlands Ship Model Basin (NSMB Publication No. 345), 1970.
30. Oosterveld MWC. Ducted propeller characteristics. In: *RINA symposium on ducted propellers*, London, 1973.
31. Pivano L, Johansen TA and Smogeli ØN. A four quadrant thrust estimation scheme for marine propellers: theory and experiments. *IEEE T Contr Syst T* 2009; 17(1): 215–226.
32. HydroComp. Correlating  $K_T/K_Q$  for symmetric-section propellers. *HydroComp Technical Report 132*. Durham, NH: HydroComp.
33. Saunders HE. *Hydrodynamics in ship design*, vol. 2. Society of Naval Architects and Marine Engineers (SNAME), 1957. Publisher: New York: Society of Naval Architects and Marine Engineers.
34. Lee SK. CFD simulation for propeller four-quadrant flows. *ABS Technical Papers*, 2006. Jersey City, NJ: Society of Naval Architects and Marine Engineers (SNAME).
35. Furlani EP, Wang R and Kusnadi H. A three dimensional model for computing the torque of radial couplings. *IEEE T Magn* 1995; 31(5): 2522–2526.
36. Furlani EP. Formulas for the force and torque of axial couplings. *IEEE T Magn* 1993; 29(5): 2295–2301.
37. Brown MW. *Seals and sealing handbook*. Elsevier Advanced Technology, 1995.



- 
38. Zou J, Qi W, Xu Y, et al. Design of deep sea oil-filled brushless DC motors considering the high pressure effect. *IEEE T Magn* 2012; 48(11): 4220–4223.
  39. Technical documentation available online at <http://www.maxonmotor.com>
  40. Empire Magnetics, Inc. <http://www.empiremagnetics.com>
  41. Evans J. Air vs oil filled sewage pump motors, <http://www.pumped101.com/oilvsair.pdf>
  42. Yoerger DR, Cooke JG and Slotine JE. The influence of thruster dynamics on underwater vehicle behavior and their incorporation into control system design. *IEEE J Oceanic Eng* 1990; 15(3): 167–178.
  43. Manfrida G and Stecco S. *Le Turbomacchine*. Pitagora Editrice, 1998. PITAGORA EDITRICE BOLOGNA (Bologna, Italy).
  44. Allotta B, Costanzi R and Monni N, H.A. Mang and J. Eberhardsteiner and H.J. Bohm and F.G. Rammerstorner. Design and simulation of an autonomous underwater vehicle. In: European congress on computational methods in applied sciences and engineering (ECCOMAS 2012) (ed J Eberhardsteiner, et al.), 6th European Congress on Computational Methods in Applied Sciences and Engineering, ECCOMAS 2012; Vienna; Austria; 10 September 2012 through 14 September 2012.
  45. B. Allotta, L. Pugi, F. Bartolini, R. Costanzi, A. Ridolfi, N. Monni, J. Gelli, G. Vettori: The Thesaurus Project, a long range AUV for extended exploration, surveillance and monitoring of archaeological sites, V International Conference on Computational Methods in Marine Engineering, ECCOMAS MARINE 2013, Hamburg, Germany, 29–31 May 2013.
  46. Singh H, Yoerger D and Bradley A. Issues in AUV design and deployment for oceanographic research. In: Proceedings of the 1997 IEEE international conference on robotics and automation, Albuquerque, NM, April 1997.